RESEARCH ARTICLE

Island Arc WILEY

Age, petrogenesis, and tectonic implications of the late Permian magmatic rocks in the Middle Gobi volcanoplutonic Belt, Mongolia

Ariuntsetseg Ganbat[1,2,3] 🔘 | Tatsuki Tsujimori[2,4] 🔘 | Laicheng Miao[5] 🔘 |
Inna Safonova[6,7] 🔘 | Daniel Pastor-Galán[4,8,9] 🔘 | Chimedtseren Anaad[3,10] 🔘 |
Shogo Aoki[11,12] 🔘 | Kazumasa Aoki[12] 🔘 | Munkhnasan Chimedsuren[13]

[1]Department of Earth Science, The University of Hong Kong, Hong Kong Island, Hong Kong SAR

[2]Department of Earth Science, Graduate School of Science, Tohoku University, Sendai, Japan

[3]Geoscience Center, Mongolian University of Science and Technology, Ulaanbaatar, Mongolia

[4]Center for Northeast Asian Studies, Tohoku University, Sendai, Japan

[5]Institute of Geology and Geophysics, Chinese Academy of Sciences, Beijing, China

[6]Novosibirsk State University, Novosibirsk, Russia

[7]Sobolev Institute of Geology and Mineralogy, Novosibirsk, Russia

[8]Frontier Research Institute for Interdisciplinary Sciences, Tohoku University, Sendai, Japan

[9]Department of Geodynamics, University of Granada, Granada, Spain

[10]Natural History Museum of Mongolia, Ulaanbaatar, Mongolia

[11]Graduate School of International Resource Sciences, Akita University, Akita, Japan

[12]Center for Fundamental Education, Okayama University of Science, Okayama, Japan

[13]"Geo-Erin" LLC, Ulaanbaatar, Mongolia

Correspondence
Ariuntsetseg Ganbat, The University of Hong Kong, Department of Earth Science, Hong Kong.
Email: ariun.0602@gmail.com

Funding information
Japan Society for the Promotion of Science, Grant/Award Numbers: JP18H01299, JP19K04043, JP21H01174; National Natural Science Foundation of China, Grant/Award Number: 41772230; Russian Science Foundation, Grant/Award Number: 21-77-20022

Abstract

The Mongol–Okhotsk Belt, the youngest segment of Central Asian Orogenic Belt, was formed by the evolution and closure of the Mongol–Okhotsk Ocean. The oceanic closure formed two volcanoplutonic belts: Selenge Belt in the north and the Middle Gobi Belt in the south (in present day coordinates). However, the origin and tectonic evolution of the Mongol–Okhotsk Belt in general, and the origin and formation age of the Middle Gobi Belt in particular, remain enigmatic. To better understand the history of the magmatic activity in the Middle Gobi Belt, we conducted geochemical, U–Pb geochronological, zircon Hf, and whole-rock Nd isotopic analyses of samples from the Mandalgovi volcanoplutonic suite, the major component of the Middle Gobi Belt. Our results show that the plutonic rock consists of ∼285 Ma gabbro, ∼265 Ma biotite-granite and ∼250 Ma hornblende-granodiorite. The volcanic counterpart is represented by a Permian Sahalyn gol rhyolite and ∼247 Ma Ikh khad andesite. The geochemical compositions of biotite-granite and hornblende-granodiorite indicate that their precursors were metagraywacke and amphibolite, respectively. They are characterized by positive whole-rock $\varepsilon_{Nd}(t)$ and zircon $\varepsilon_{Hf}(t)$ values, indicating juvenile protoliths. The gabbro was derived by partial melting of a metasomatized lithospheric mantle source in a supra-subduction setting. The biotite-granite and Sahalyn gol

rhyolite are formed by remelting of sediments in an inter-arc extension setting. Later the hornblende-granite and Ikh khad volcanic were emplaced at a volcanic arc formed by the subduction of the Mongol–Okhotsk Ocean. We conclude that the magmatic rocks of the Middle Gobi Belt formed in an active continental margin setting. Considering the consistent distribution of coeval arc-derived magmatic formations along the southern margin of the Mongol–Okhotsk Belt, the oceanic basin was closed in a relatively simultaneous manner.

KEYWORDS
CAOB, Mongol–Okhotsk Belt, peraluminous granite, U–Pb geochronology, Zircon Hf isotope

1 | INTRODUCTION

The growth of the continental crust has represented one of the most exciting debates in the Earth Sciences for at least the last three decades (e.g., Belousova et al., 2010; Ganbat, Tsujimori, Boniface, et al., 2021; Jahn et al., 2000; Kemp et al., 2007; Kröner et al., 2014, 2017; Rino et al., 2008; Taylor & McLennan, 1985). Pioneering research pointed out that the formation of continental crust was episodical and most of its volume formed in the Precambrian (e.g., Armstrong, 1981). However, more recent studies suggest that significant continental growth took place during the Phanerozoic (Hawkesworth et al., 2010; Jahn, 2004; Rosembaum, 2018; Safonova, 2017). Understanding the continental growth during the Phanerozoic can provide crucial knowledge on the mechanisms of magmatic differentiation from the mantle to the crust, as well as important perceptions about the compositions and evolution of the continental crust.

The Central Asian Orogenic Belt (CAOB) is the world's largest accretionary orogen preserved, with more than 800 Ma of tectonic history since the Neoproterozoic, formed by oceanic subduction accompanied by multiple accretions of island-arcs, seamounts, and microcontinents to the active margins of the Siberian and Kazakhstan continents, their collision, and amalgamation during the closure of the Paleo-Asian Ocean in the late Paleozoic, and the Mongol–Okhotsk Ocean (MOO) in the early Mesozoic (Figure 1, inset map) (e.g., Buslov et al., 2001; Dobretsov et al., 1995; Safonova, 2017; Safonova et al., 2011; Wilhem et al., 2012; Windley et al., 2007; Xiao et al., 2003; Yakubchuk, 2017). The CAOB is also the locus of rapid and extensive juvenile granitic formation during the Phanerozoic, but the petrogenesis, geodynamics, and relationships with CAOB's crustal growth are controversial (Jahn, 2004; Kröner et al., 2014; Safonova, 2017). A classical view of the CAOB holds that nearly half of the granites of the CAOB formed after the successive accretion of juvenile arc complexes and subduction accretion during the Phanerozoic (Sengör, 1990). Another view proposes that the Phanerozoic CAOB granitoids were the product of basaltic underplating in a post-collisional setting (Jahn et al., 2000; Jahn et al., 2009; Wu et al., 2011). Nonetheless, the origins of the CAOB's granitoids might be far more complex. Some authors pointed out that many key features are explicable by Paleozoic ridge subduction (e.g., Tang et al., 2012; Windley & Xiao, 2018).

The Mongol–Okhotsk Ocean (MOO) was the youngest oceanic basin, of which closure finalized the welding of CAOB terranes (Arzhannikova et al., 2022; Kravchinsky et al., 2002; Sorokin et al., 2020). The oceanic crust of the MOO was subducting to the north, under the Siberian continent, and to the south, under the Central Mongolia–Erguna block/terrane. The subduction resulted in the formation of volcanoplutonic belts extended from Central Mongolia to NE China (Figure 2; e.g., Ganbat, Tsujimori, Miao et al., 2021; Liu et al., , 2018; Zhao et al., 2017; Zhu et al., 2016, 2022). The subduction under the Siberian continent was active until the oceanic closure and resulted in the formation of the Carboniferous–Jurassic granitic belts in NW Mongolia and Western Transbaikalia. Recent studies have shown two main episodes of magmatism related to the southward subduction, which formed the Permian Monhhaan granitoids in NE Mongolia (Figure 2; Zhao et al., 2017) and the Triassic granitoids in the Erguna, Xing'an massives in NE China (e.g., Liu & Zhao, 2018; Tang et al., 2016). However, these studies were focused on the eastern part of the belt and have provided little constraints from the southern volcanic rocks and mafic intrusions. Thus, the geodynamic evolution of the southern margin of the MOO remains obscure, in particular, whether it was active during a relatively short period or throughout the whole period of oceanic closure. This study fills this gap and presents new radiogenic ages to provide new insights into the evolution and closure of the MOO.

The volcanoplutonic belts in the territory of Mongolia, namely Selenge and Middle Gobi, on its northern and southern sides (in actual coordinates), respectively (Figure 1; Zorin, 1999; Parfenov et al., 2001). The Middle Gobi Belt is thought to represent the southern active margin of the MOO (Figure 1), however, it has a deficiency in detailed structural studies and up-to-date radiogenic ages and geochemical data. In this study, we present new zircon U–Pb ages, zircon Hf isotope, and whole-rock geochemical and Nd isotope data from igneous rocks of the Mandalgovi volcanoplutonic suite of the Middle Gobi Belt. We will discuss the ages and tectonic settings of their emplacement, and petrogenesis in order to contribute to a better understanding of the crustal growth and tectonic evolution of the MOO.
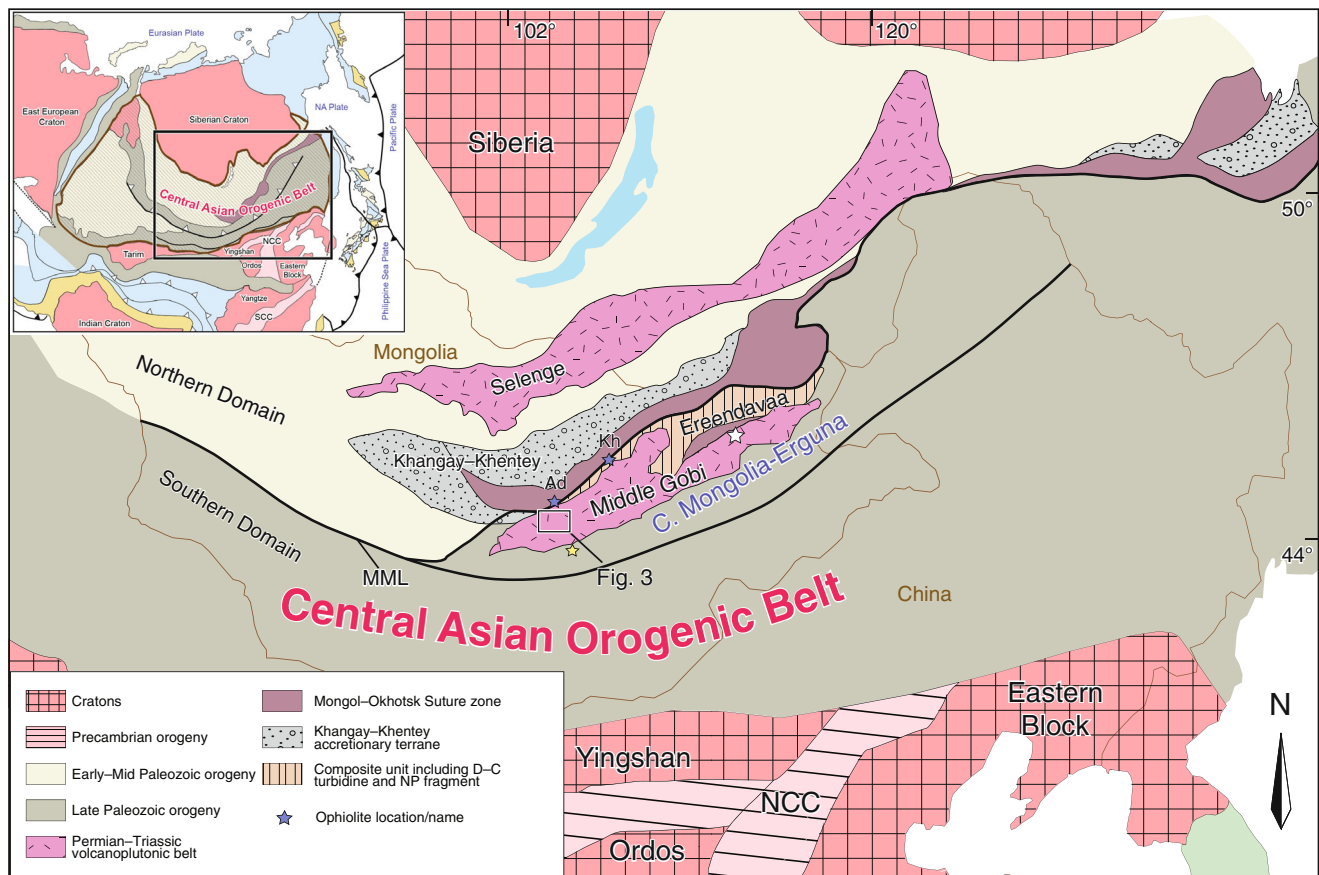
FIGURE 1 Sketch map illustrating the major tectonic units along the Mongol–Okhotsk Belt (modified after Khanchuk et al., 2015; Miao et al., 2020). Inset map showing the location of the CAOB (modified after Safonova, 2017). NCC, Northern China Craton; MML, Main Mongolian Lineament. Ophiolites: Ad, Adaatsag; Kh, Khukh davaa

2 | GEOLOGICAL SETTING

2.1 | Geological background of Mongolia

Mongolia is located in the central CAOB (Figure 1), and has recorded multiple episodes of orogeny during the Neoproterozoic to the late Paleozoic (e.g., Badarch et al., 2002; Rojas-Agramonte et al., 2011; Windley et al., 2007). Geologically, Mongolia consists of a Northern Domain and a Southern Domain separated by the Main Mongolian Lineament (Badarch et al., 2002; Tomurtogoo et al., 2005; Figure 1). The Northern Domain comprises Neoproterozoic–early Paleozoic accretionary units and a collage of collided Precambrian blocks (Badarch et al., 2002; Wilhem et al., 2012; Xiao et al., 2003). The Southern Domain includes relicts of an extended long-lived subduction–accretionary system of the Paleo-Asian Ocean, which was active from the Neoproterozoic to the Permian (e.g., Batsaikhan et al., 2018; Demoux et al., 2009; Kröner et al., 2010). From late Paleozoic to Mesozoic time, the Southern Domain approached and eventually docked with the Northern Domain to close MOO.

2.2 | The Mongol–Okhotsk Belt

The Mongol–Okhotsk Belt extends from central Mongolia to the Okhotsk Sea over 3000 km. Its formation is linked with the evolution of the MOO. The Mongol–Okhotsk suture zone is marked by the ca. 325–314 Ma Adaatsag–Khukhu Davaa ophiolites (Tomurtogoo et al., 2005; Zhu et al., 2018) (Figures 1 and 2). The MOO opened in late Ordovician–early Silurian times, possibly as a back-arc basin on the northern (in present coordinates) active margin of the Paleo-Asian Ocean near the Central Mongolia–Erguna block (Bussien et al., 2011; Miao et al., 2020; Winkler et al., 2020).

Paleomagnetic data suggest that the final closure of the MOO occurred in the early Cretaceous (e.g., Metelkin et al., 2010), whereas the sedimentary records show that the ocean has closed in early–late Mesozoic time (e.g., Arzhannikova et al., 2022; Cogné et al., 2005; Sorokin et al., 2020). There is a well-known scissor-style kinematic model of ocean closure, which is reflected by the younging trend of sediments and intrusions along the suture zone from west to east (e.g., Metelkin et al., 2010; Xiao et al., 2015). However, a recent model argues against the scissor-like closure model and proposes that different segments of the ocean closed
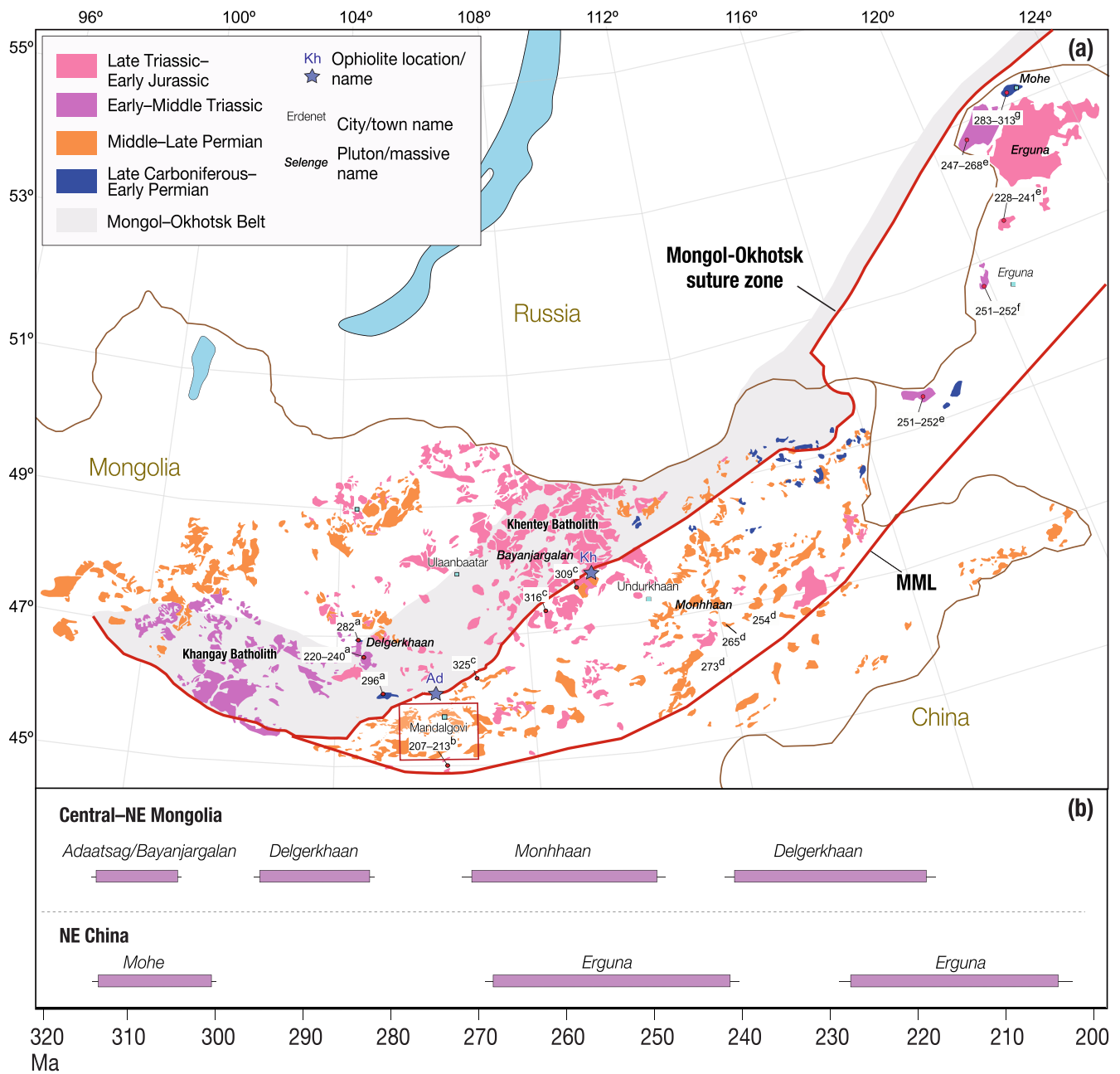
FIGURE 2 (a) Late Paleozoic–early Mesozoic granitic distribution in Central–NE Mongolia and NE China. Published late Paleozoic–early Mesozoic U–Pb ages of Central Mongolia–Erguna are also shown. a—Ganbat, Tsujimori, Miao et al. (2021); b—Zhu et al. (2016); c—Zhu et al. (2022); d—Zhao et al. (2017); e—Tang et al. (2016); f—Li et al. (2017); g—Liu et al. (2018). (b) Timeline of published ages in late paleozoic–early mesozoic U–Pb ages in Central–NE Mongolia and NE China. Presented ages are interpreted as related with the evolution of the Mongol–Okhotsk Ocean in corresponding references

independently, depending on the initial shape of the paleo-continental margins (Arzhannikova et al., 2022).

The Mongol–Okhotsk suture zone is bounded by the Khangay–Khentey terrane in the northwest (Figure 1; Kelty et al., 2008; Bussien et al., 2011; Ruppen et al., 2014). The Khangay–Khentey terrane hosts all typical units of Ocean Plate Stratigraphy (OPS; from bottom to top): oceanic basalt (MORB, OIB), radiolarian pelagic chert, hemipelagic siliceous mudstone, siltstone, thick trench turbidite, and sandstone (e.g. Dagva-Ochir et al., 2020; Safonova et al., 2009). The provenance

analysis of sandstones and the U–Pb ages of detrital zircons show that the sediments of the northern part deposited from the Silurian to early Carboniferous times in a subduction–accretion setting, which apparently stopped in the Carboniferous. Later, subduction was re-initiated during the Permian sandstone (e.g., Kelty et al., 2008; Ruppen et al., 2014).

The Selenge and Middle Gobi belts are abutting with the Khangay–Khentey terrane (Figure 1). Selenge Belt is believed to represent the northern, (Figure 1), and the Middle Gobi Belt is the
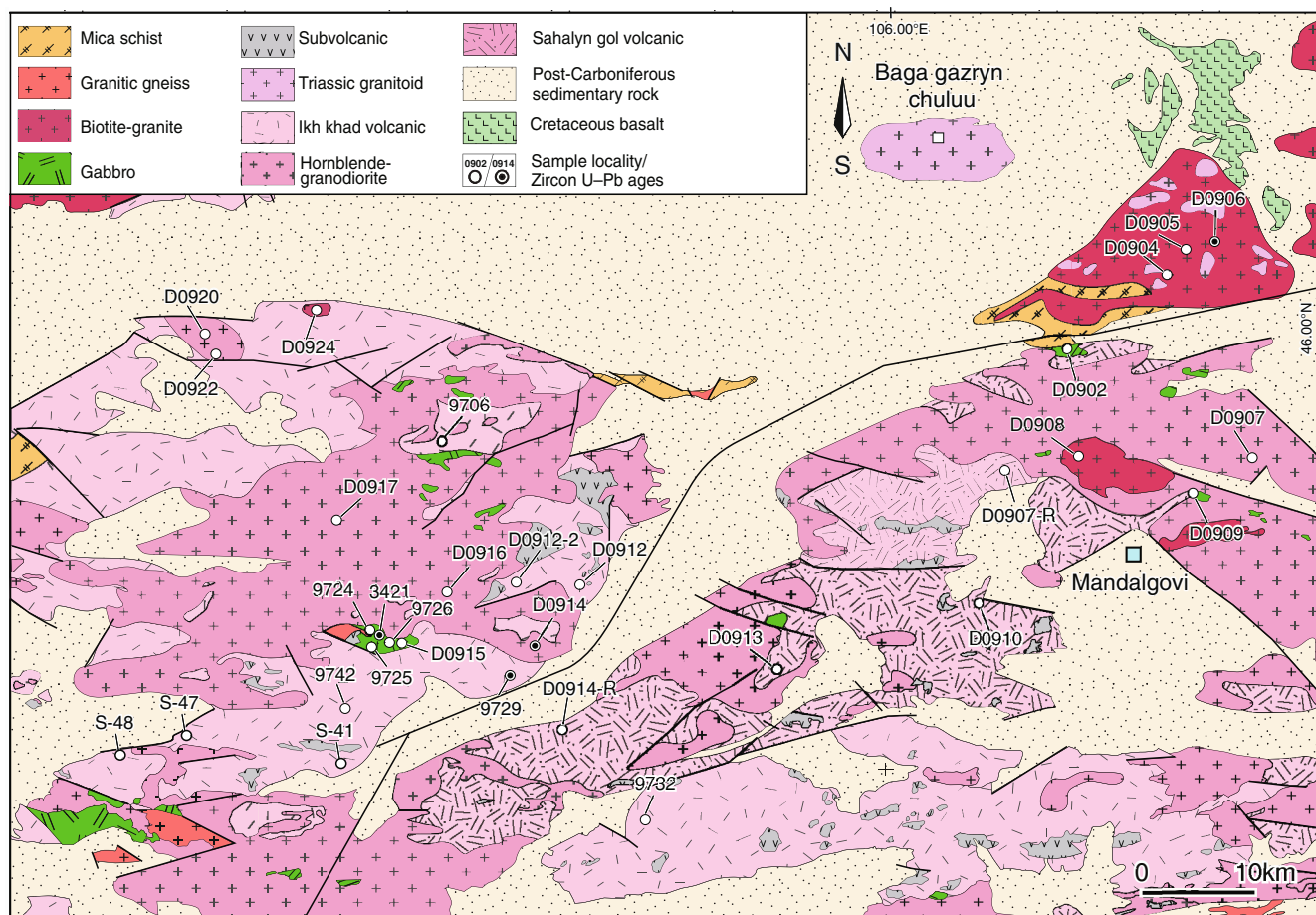
FIGURE 3 Simplified geological map of the Mandalgovi area of the Middle Gobi Belt (modified after the 1:200 000 state geological map), showing sample locations

southern active margin of the MOO (Parfenov et al., 2001; Zorin, 1999). The southern part of the Khangay–Khentey terrane experienced a back-arc extension during the early Paleozoic (Bussien et al., 2011; Winkler et al., 2020), and from the Devonian and to early Carboniferous it evolved as a passive margin. In the late Carboniferous, the subduction re-initiated resulting in the transportation of detrital zircons from volcanic rocks and plutons of the Middle Gobi Belt until the Triassic (Bussien et al., 2011; Kelty et al., 2008).

2.3 | The Middle Gobi Belt

The Middle Gobi Belt is a magmatic domain located south of the Mongol–Okhotsk suture zone (Figure 1) (Badarch et al., 2002), and contains Precambrian basement rocks as the bulk of the crust. The Precambrian basement consists of Meso–Neoproterozoic quartz-feldspathoid gneisses, metamorphic schists, pelitic gneisses, and metasandstones and marbles (Figure 3) overlain by the Silurian and Devonian marine sedimentary and volcanic rocks (turbiditic and pelagic series), which are intruded and overlapped by Permian plutonic and volcanic rocks, respectively (Badarch et al., 2002).

The Middle Gobi volcanoplutonic belt is dominated by Permian calc-alkaline andesites, dacites, rhyolites, trachyrhyolites, and subalkaline granites (Gerel et al., 2019; Khanchuk et al., 2015). The emplacement of ~270 Ma peraluminous granites and their associated volcanics, and ~240 Ma metaluminous granites (Gerel et al., 2019; Machowiak et al., 2012) was related to the subduction of the MOO lithosphere (e.g., Zhao et al., 2017, 2020). The late Triassic (~210 Ma) bimodal volcanic suites and coeval A-type granites were interpreted to form in a back-arc setting due to the rollback of the MOO slab (Zhu et al., 2016).

The magmatic rocks are distributed in the Mandalgovi area, at the western fringe of the Middle Gobi Belt, and occupy a large area of 250 × 650 km² (Figure 3; Gerel et al., 2019). The magmatic rocks consist of late Carboniferous mafic–felsic volcanics (325 Ma dacite) and an intrusion (316–305 Ma gabbro and granite) (Zhu et al., 2022). They are unconformably overlain by Permian volcanics, volcaniclastics, clastic rocks, and gneissic migmatites, which co-exist with Mandalgovi gabbro, gabbro-diorites, granitoids (Figure 3; Badarch et al., 2002). These rock associations are covered by Jurassic to Cretaceous sedimentary rocks (conglomerate, sandstone, and gravelite) and (volcanics basalts, basaltic andesites, andesites, and rhyolites) (Figure 3).

3 | ANALYTICAL METHODS

3.1 | U–Pb geochronology

Zircon crystals were separated in the Graduate School of Science, Tohoku University, using standard techniques including conventional rock-crushing, magnetic and heavy liquid separation, and handpicking under a binocular microscope. Then, zircon crystals of similar size were mounted in epoxy discs. Zonation of zircon interiors was documented using cathodoluminescence (CL) imaging with a Hitachi S-3400 N scanning electron microscope, equipped with a Gatan MiniCL. In-situ zircon U–Pb dating was carried out at the Okayama University of Science using a Thermo Fisher Scientific iCAP-RQ quadrupole inductively coupled plasma mass spectrometer coupled to a Teledyne Cetac Technologies Analyte G2 ArF excimer laser ablation (LA) system equipped with a HelEx 2 volume sample chamber. The laser ablation was conducted at the laser spot size of 25 μm, the fluence of 1.8 J/cm², and the repetition rate of 5 Hz. Zircon standard Nancy 91500 (1065 Ma; Wiedenbeck et al., 2004) was used for age calibration, NIST SRM 612 standard (Jochum et al., 2011) for instrument optimization, and Plešovice zircons (337 Ma; Sláma et al., 2008) as secondary standards for quality control. U–Pb ages and concordia diagrams were, respectively, calculated and plotted using the program IsoplotR (ver. 3.75; Vermeesch, 2018); the concordia age of each sample incorporates errors on the decay constants and includes evaluation of concordance of apparent ages. The concordia ages and errors are at the two-sigma level.

3.2 | Whole-rock geochemistry

Twenty-eight samples were selected for whole-rock analysis. Concentrations of major and trace elements were measured at Activation Laboratories Ltd., Canada, using Code 4Litho Lithogeochemistry Package with fusion inductively coupled plasma optical emission spectrometry (FUS-ICPOES) and inductively coupled plasma mass spectroscopy (FUS-ICPMS), respectively. One more sample was analyzed at the Analytical Center for Multi-Element and Isotope Studies of the Institute of Geology and Mineralogy, Novosibirsk, Russia. Concentrations of major oxides were determined by the X-ray fluorescence (XRF) method using an Applied Research Laboratories ARL-9900-XP, following the standard procedure. Trace elements for eighteen samples were analyzed by mass spectrometry with inductively coupled plasma (ICPMS) after fusion with LiBO₂. Simultaneous determination of all elements was carried out to low, medium, and high resolution, on a Finnigan Element-II high-resolution mass spectrometer with external calibration using BHVO-1 reference samples and an internal standard. The method has been validated through the analysis of reference materials. Reference materials NIST 694, W-2a, BIR-1a are for major and trace elements, and NCS DC70014, LKSD 3 for REE. Relative standard deviations for all elements were <10% within the determined concentration ranges.

3.3 | Zircon Hf isotopes

Hf isotope analysis was carried out using a Thermo Fisher Scientific Neptune Plus multi-collector (MC)-ICPMS in combination with a Geolas 2005 excimer ArF laser ablation system (193 nm) at the Institute of Geology and Geophysics, Chinese Academy of Science, Beijing. The analyses for zircon grains from the granites were conducted with a beam diameter of 63 μm, a 6 Hz repetition rate, and an energy of 15 mJ/cm². This setting yielded a signal intensity of 10 V at ^{180}Hf for the standard zircon Nancy 91500. The typical ablation time was 26 s, resulting in pits 20–30 μm deep. The initial ^{176}Hf/^{177}Hf ratios for the unknown samples were calculated to their initial value, using the measured ^{176}Lu/^{177}Hf ratios, the apparent age of each zircon grain, and an ^{176}Lu decay constant of 1.867×10^{-11} year^{-1} (Söderlund et al., 2004). Epsilon Hf were calculated using a present-day chondritic ^{176}Hf/^{177}Hf value of 0.282785 and ^{176}Lu/^{177}Hf of 0.0336 (Bouvier et al., 2008) and the present-day felsic crustal ratio of ^{176}Lu/^{177}Hf = 0.015.

3.4 | Sm–Nd isotopic analysis

Sm–Nd isotopic analyses were performed at the Institute of Geology and Geochronology, Russian Academy of Sciences, Saint-Petersburg. About 100 mg of whole-rock powder was dissolved in a mixture of HF, HNO₃, and HClO₄. A ^{149}Sm–^{150}Nd spike solution was added to all samples before dissolution. REEs were separated on BioRad AGW50-X8 200–400 mesh resin using conventional cation-exchange techniques. Sm and Nd were separated by extraction chromatography with a LN-Spec (100–150 mesh) resin. The total blank in the laboratory was 0.1–0.2 ng for Sm and 0.1–0.5 ng for Nd. Isotopic compositions of Sm and Nd were determined on a TRITON TIMS mass-spectrometer. The precision (2σ) of Sm and Nd contents and ^{147}Sm/^{144}Nd ratios were 0.5% and 0.005% for ^{143}Nd/^{144}Nd ratios. ^{143}Nd/^{144}Nd ratios were adjusted relative to a value of 0.512115 for the JNdi-1standard. During the period of analysis, the weighted average of 10 analysis JNdi-1 Nd standard runs yielded 0.512108 ± 7 (2σ) for ^{143}Nd/^{144}Nd, normalized against ^{146}Nd/^{144}Nd = 0.7219. The $\epsilon_{Nd}(t)$ values were calculated using the present-day values for a chondritic uniform reservoir (CHUR) ^{143}Nd/^{144}Nd = 0.512638 and ^{147}Sm/^{144}Nd = 0.1967 (Jacobsen & Wasserburg, 1984). Whole-rock Nd model ages $T_{Nd(DM)}$ were calculated using the model of Goldstein and Jacobsen (1988) according to which the Nd isotopic composition of the depleted mantle evolved linearly since 4.56 Ga ago and has a present-day value $\epsilon_{Nd}(0)$ of +10 (^{143}Nd/^{144}Nd = 0.513151 and ^{147}Sm/^{144}Nd = 0.21365). Two-stage (crustal) Nd model ages $T_{Nd(C)}$ were calculated using a mean crustal ratio ^{147}Sm/^{144}Nd of 0.12.

4 | RESULTS

4.1 | Petrography

Mineral assemblages of representative samples are given in Table 1.

TABLE 1 Mineral assemblage and contents of studied samples of the Middle Gobi Belt

| | Sample | Lithology | Mineral content, vol% | | | | | | |
			Qz	Kfs	Pl	Bt	Hbl	Cpx	Accessory mineral
⌣285 Ma gabbro-diorite, gabbro	D0902	Gabbro-diorite			⌣50	⌣10	⌣35		⌣3
	D0909-2	Gabbro-diorite			⌣50	⌣10	⌣35		⌣2
	9724	Gabbro			⌣50		⌣20	⌣20	⌣3
Lower Permian Sahalyn gol volcanic	D0910	Rhyolite	⌣10	⌣5	⌣5	⌣2			⌣2
	D0913	Rhyolite	⌣10	⌣5	⌣5	⌣5			⌣2
	D0907-R	Rhyolite	⌣10	⌣10	⌣10	⌣5			⌣2
⌣265 Ma Biotite-granite	D0904	Monzogranite	⌣40	⌣35	⌣35	⌣5			⌣2
	D0905	Monzogranite	⌣35	⌣35	⌣25	⌣15			⌣3
	D0908	granite	⌣25	⌣25	⌣35	⌣15			⌣3
⌣247 Ma Ikh khad volcanic	D0912	Dacite			⌣20	⌣10			⌣2
	S-41	Andesite			⌣50		⌣10		⌣2
	S-47	Dacite	⌣10	⌣10	⌣40				⌣2
	S-48	Dacite		⌣20	⌣40		⌣10		⌣2
	9706	Rhyolite	⌣20	⌣10	⌣20		⌣10		⌣2
	9742	Basaltic andesite			⌣50			⌣5	1
⌣250 Ma Hornblende-granodiorite	D0907	Granite	⌣35	⌣35	⌣35		⌣10		⌣3
	D0914	Granodiorite	⌣20	⌣35	⌣40		⌣10		⌣3
	D0917	Granodiorite	⌣20	⌣20	⌣50		⌣10		⌣3
	D0922-1	Granodiorite	⌣2⌣5	⌣15	⌣50		⌣10		⌣3

Abbreviations: Qz, quartz; Kfs, K-feldspar; Pl, plagioclase; Hbl, hornblende; Cpx, clinopyroxene.

A gabbro-diorite sample (D0909) has a hypidiomorphic texture. The major minerals are plagioclase (50%–55%), hornblende (25%–30%), and biotite (15%–20%) (Figure 4a). Euhedral to subhedral plagioclase exhibits polysynthetic twinning zoning, and kinking, and is partially replaced by sericite. Accessory minerals are ilmenite, magnetite, and apatite. A gabbro (Sample-3421; Figure 4b) characterized by gabbroic texture and consists of medium-coarse grained anhedral plagioclase (40%–60%), pale-green clinopyroxene (10%–20%), greenish hornblende replaced pyroxene (10%–20%) and accessory biotite, serpentine, chlorite and epidote.

A biotite-granite sample (D0906; Figure 4c), includes quartz (30%–35%), plagioclase (30%–35%), K-feldspar (20%–25%), and biotite (15%–20%). Plagioclase and K-feldspar occur as porphyritic minerals and biotite is common in fractures and along plagioclase boundaries (Figure 4d). Accessory minerals are magnetite, apatite, and zircon. A hornblende-granite sample (D0914) is coarse- to fine-grained hypidiomorphic granodiorite consisting of subhedral to anhedral plagioclase (40%–45%), K-feldspar (20%–25%), subhedral quartz (15%–20%), euhedral hornblende (15%–20%) and biotite (5%–10%) (Figure 4e, f) plus accessory zircon and opaque minerals and secondary sericite and chlorite.

A porphyritic granodiorite (D0920) (Figure 4f) comprises euhedral plagioclase (35%–40%), orthoclase (15%–20%), and hornblende (10%–20%) and quartz (10%–20%) as phenocrysts. The accessory minerals are zircon, apatite, and titanite. Hornblende is replaced by chlorite and epidote. Plagioclase exhibits carlsbad and polysynthetic twinning and is partially altered to saussurite. Orthoclase shows carlsbad and albite twinning, in places, it is cut by epidote veins and altered to sericite.

An andesite (9729) (Figure 4g) has a porphyritic texture and carries phenocrysts of plagioclase and hornblende (20%–30%). The groundmass consists of plagioclase, clinopyroxene, and accessory minerals. The elongated prismatic plagioclase phenocrysts are characterized by tabular idiomorphic forms and look partly altered to phyllite. Hornblende is also partially replaced by chlorite and epidote.

A rhyolite (D0914-R) (Figure 4h) has a porphyritic texture, and build-up of K-feldspar, quartz, and biotite phenocrysts (40%–50%). The groundmass (50%–60%) is dominated by fine-grained quartz and feldspar and shows pegmatitic intergrowth texture. K-feldspar has tabular and prismatic idiomorphic forms and shows perthite intergrowths. Biotite is moderately replaced by chlorite.

A dacite (9732) (Figure 4i) possesses a holocrystalline texture and consists of phenocrysts (10%–20%) of orthoclase, plagioclase, biotite, and quartz. The groundmass (70%–80%) consists of feldspar, quartz, and devitrified glass. Plagioclase phenocrysts have polysynthetic and carlsbad twinning. Biotite grains have greenish to brownish colors.

4.2 | Whole-rock major and trace element geochemistry

4.2.1 | Gabbro, gabbro-diorite

The major and trace element geochemical data of the studied samples are given in Table S1.
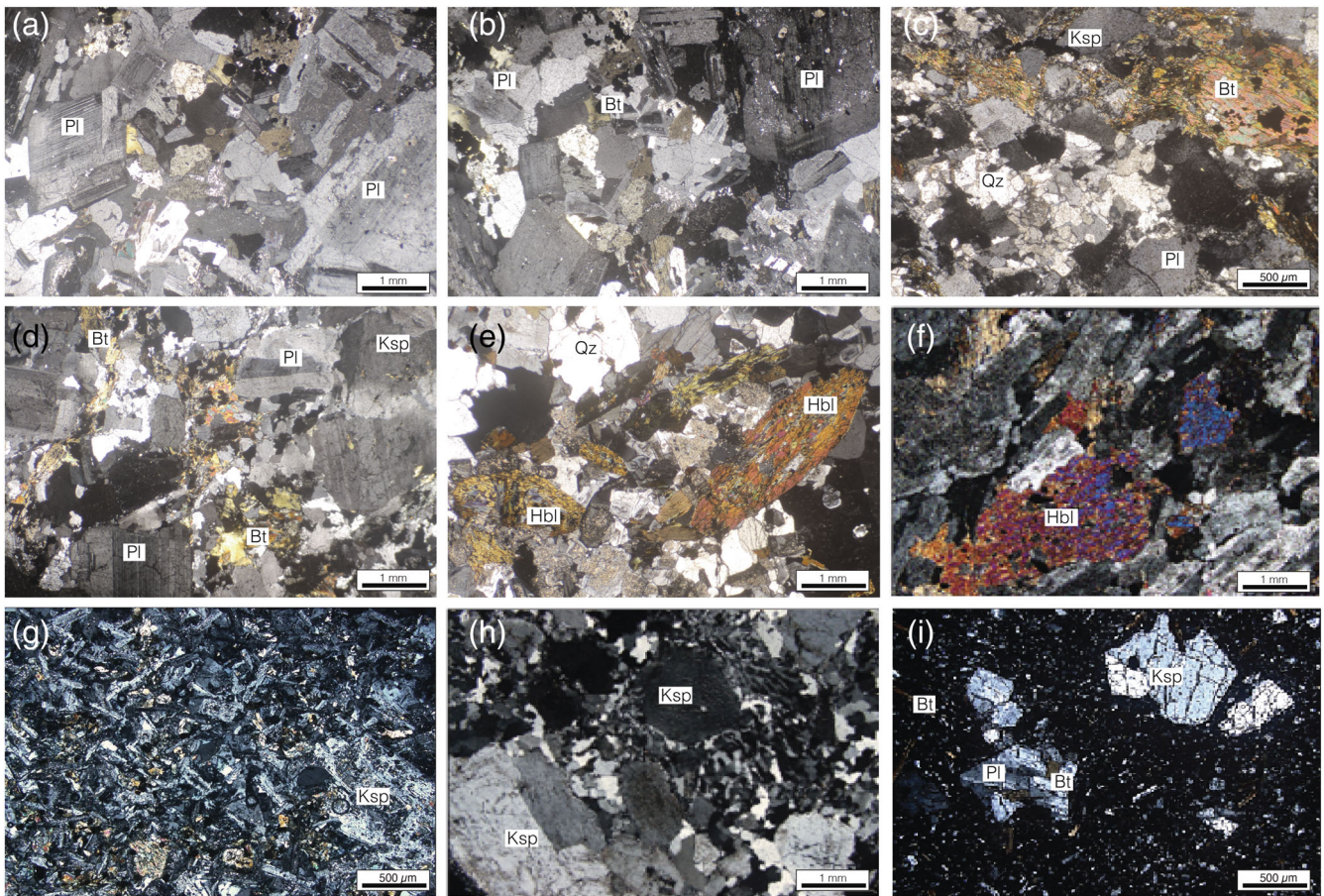
FIGURE 4 Photomicrographs of cross-polarized light view showing textures and mineral assemblage of the studied samples from the plutonic and volcanic rocks from the Middle Gobi Belt. (a, b) Gabbrodiorite (Sample D0909); (c, d) Biotite-granite (sample D0906); (e, f) Granodiorite (sample D0914); (g) Andesite (sample 9729); (h) Rhyolite (sample D0914-R); (i) Dacite (sample 9732). Bt, biotite; Hbl, hornblende; Kfs, K-feldspar; Pl, plagioclase; Qz, quartz

This group of samples includes gabbro-diorite and diorite (Figure 5a). They have relatively narrow spanned SiO_2 content (44–54 wt.%), high contents of MgO (2.74–8.8 wt.%), CaO (8.51–13.6 wt.%), FeO^T (5.2–12 wt.%), and Al_2O_3 (16.9–27.2 wt.%) and low total alkalis ($Na_2O + K_2O$ = 1.05%–4.03%) (Figure 5c). The contents of TiO_2 and P_2O_5 range from 0.4 to 1.2 wt.% and from 0.04% to 0.24%, respectively.

In terms of trace elements, the samples of gabbro-diorite display a comparably flat REE pattern [$(La/Yb)_N$ = 63–65] without significant Eu anomalies (Eu/Eu* = 0.96–1.15) (Table S1; Figure 6a), indicating no to weak fractionation and/or accumulation of plagioclase. They are characterized by lower Rb, Ba, Th, and U than the intermediate-felsic rocks of the same pluton, and characteristic troughs at Nb and Ta (Figure 6b).

4.2.2 | Biotite-granite

Biotite-granites consists have relatively narrow ranges of SiO_2 (69.2–77.3 wt.%), total alkalis ($Na_2O + K_2O$ = 6.9–8.2 wt.%), and Al_2O_3 (12–15 wt.%) (Figure 5a). They are characterized by low TiO_2

(0.14–0.18 wt.%), moderate FeO^T (1.42–1.84 wt.%), and Mg# (32–42). The granites are belong to high-K calc-alkaline (Figure 5c). According to the A/CNK versus A/NK diagram, they can be classified as peraluminous granitoids (Figure 5d). The chondrite normalized REE patterns (Figure 6a) show enrichment in LREEs [$(La/Yb)_{CN}$ = 0.7–3.6], and weak negative Eu anomalies. The multi-element patterns show negative Nb, P, and Ti anomalies (Figure 6b) and significant enrichment in K, Rb, Ba, and Pb.

4.2.3 | Sahalyn gol rhyolite

The Sahalyn gol rhyolite samples have similar major element compositions, which are characterized by similar SiO_2 (70.4–76.9 wt.%), Al_2O_3 (11.4–15.3 wt.%), CaO (0.1–1.88 wt.%), Na_2O (2.62–4.31 wt.%) and K_2O (3.36–4.53 wt.%), MgO (0.09–0.3 wt.%; Mg# = 11–41) and TiO_2 (0.12–0.26 wt.%) contents. All samples are plotted as calc-alkaline rhyolite fields (Figure 5b). The chondrite-normalized rare earth element patterns of these samples display a negative slope with depletion of HREE [$(La/Yb)_N$ = 0.7–3.4] and have Eu anomalies (Eu/Eu* = 1.01–1.04) (Figure 6c). They
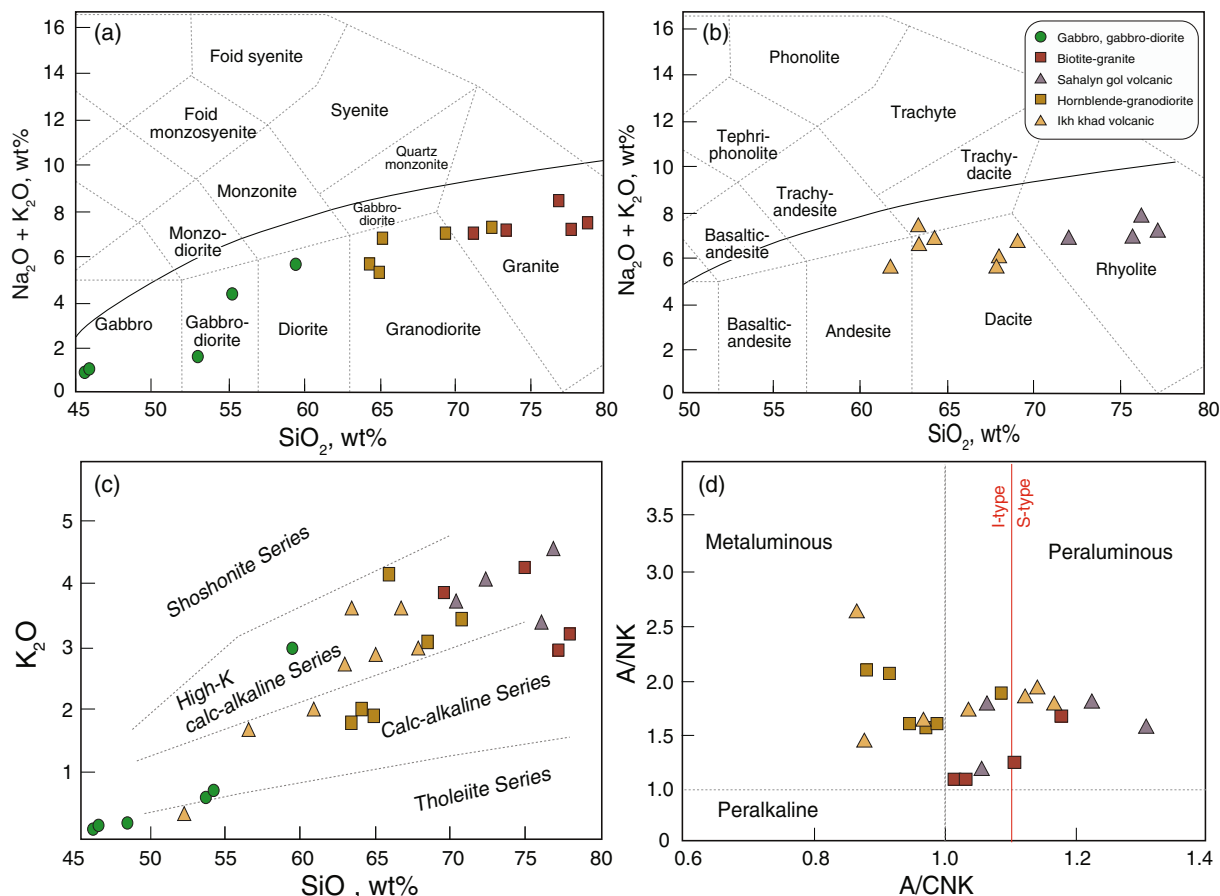
FIGURE 5 Major element discrimination diagrams showing the compositions and characteristics of the studied samples from Middle Gobi Belt. (a) SiO_2 versus ($Na_2O + K_2O$) total alkali-silica (TAS) diagram for plutonic rocks (after Irvine & Baragar, 1971), (b) SiO_2 versus ($Na_2O + K_2O$) total alkali-silica (TAS) diagram for volcanic rocks (after Le Bas et al., 1986), (c) K_2O wt% versus SiO_2 wt% plot (Peccerillo & Taylor, 1976), (d) A/CNK [molar Al_2O_3/(CaO × Na_2O × K_2O)] versus A/NK [molar Al_2O_3/(Na_2O × K_2O)] diagram, the boundary line is from Maniar and Piccoli (1989)

exhibit positive Ba, U, and Sr, but negative Nb, Ta, and Ti anomalies on primitive mantle-normalized (PM) trace element diagrams (Figure 6d).

4.2.4 | Hornblende-granodiorite

The granodiorite samples have lower SiO_2 (63–70.7 wt.%), K_2O (1.91–3.99 wt.%), and higher Al_2O_3 (13.7–17.3 wt.%), Na_2O (3.09–4.64 wt.%) and $K_2O + Na_2O$ (5.15–8.2 wt.%) than the biotite-granites. The samples are characterized by high FeO^T (3.43–5.12%), CaO (2.49–5.31%), TiO_2 (0.4–0.8%), and MgO (1.15–2.59%). Accordingly, they belong to the calc-alkaline series (Figure 5a,b; Table S1) and represent metaluminous granites (Figure 5d).

In the CI-normalized REE diagrams (Figure 6a), they exhibit various degrees of LREE enrichment with $(La/Yb)_N$ ratios of 3.5–25.4 and weak to zero negative anomalies at Eu (Eu/Eu* = 0.52–1.03). In the PM-normalized spidergrams (Figure 6b), all samples display patterns with enrichment of Rb, Th, K, La, Ce, and Zr and significant troughs at P and Ti.

4.2.5 | Ikh khad volcanic

Ikh khad volcanic samples vary from basaltic andesites to dacites (Figure 6b). They have SiO_2 contents of 52–67 wt.%, Na_2O of 0.52–5.22 wt.%, and K_2O of 0.2–5.56 wt.%, Al_2O_3 of 15.2–23.06 wt.%, TiO_2 of 0.5–1.09 wt.% and CaO of 1.8–6.82 wt.%. The MgO and FeO^T contents range from 0.89 to 2.88 wt.% and from 5.41 to 14.45 wt.%, respectively, yielding Mg# values between 29 and 60. All samples are plotted in the calc-alkaline field (Figure 6b). Ikh khad rhyolites have high LREE/HREE ratios of $(La/Yb)_N$ of 7.62–8.62 and no to weak negative Eu anomalies (Figure 7a). In a PM normalized trace element variation diagram, the samples are enriched in LILE and LREEs and have strongly negative anomalies in Nb, Ta, and Ti (Figure 6b).

4.3 | Geochronology

A gabbro (Sample 3421): colorless euhedral to subhedral zircons are shorter than 200 μm, stubby in shape with aspect ratios not exceeding 2, and exhibit fine-scaled oscillatory zoning in CL-images (Figure 7a).
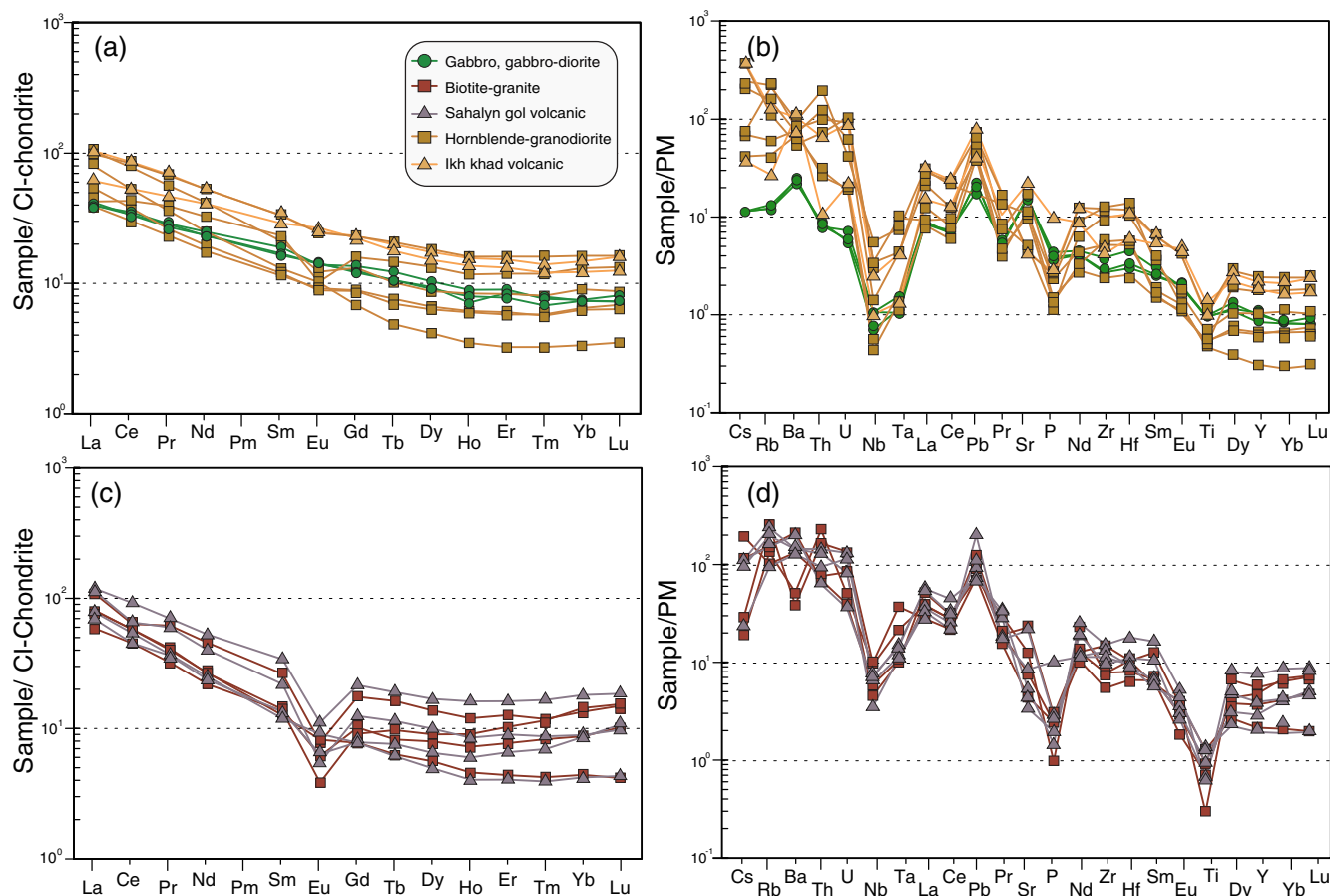
FIGURE 6 CI-chondrite-normalized REE patterns and primitive-mantle-normalized trace element spidergrams for the studied samples from the Middle Gobi Belt. Both chondrite and primitive-mantle normalized values are from Sun & McDonough (1989)

We analyzed seven zircons with Th/U ratios ranging from 0.37 to 1.27. All analyzes plot on the concordia diagram, providing an age of 285 ± 3.3 Ma (MSWD = 4.5; Figure 8a), which is interpreted as the crystallization age of the gabbro.

A biotite-granite (Sample D0906): Zircons were colorless or light yellow and are stubby or euhedral to anhedral, about 100–300 μm in size, elongation ratio 1–3. CL images show fine-scaled oscillatory zoning and rare unzoned xenocrystic cores (Figure 7b). Fourteen analyses show the contents of U and Th varying from 67 to 175 μg/g and from 57 to 204 μg/g (Table 2), respectively, with Th/U ratios ranging from 0.6 to 1.2. The U–Pb ratios give a concordia age of 265 ± 2 Ma (MSWD = 0.19, Figure 8b), which is interpreted as the crystallization age of biotite-granite.

A hornblende-granodiorite (Sample D0914): Zircons are colorless or light brown, euhedral to subhedral, and stubby prisms up to 200 μm long with aspect ratios not exceeding 2 and exhibit fine oscillatory zoning (Figure 7c). Sixteen analyses of zircons show the contents of U and Th varying from 143 to 236 μg/g and from 136 to 300 μg/g, respectively, and the ratios of Th/U ranging from 0.9 to 1.3. All analyses were plotted on or near the concordia and yielded an age of 250 ± 3 Ma (MSWD = 1, Figure 8c). This age is interpreted to represent the crystallization age of hornblende granodiorite.

An andesite (Sample 9729): up to 200 μm long transparent to light brown zircons are stubby to elongated with aspect ratios from 1 to 3. The CL image shows wide oscillatory zoning, some zircons have homogeneous xenolith cores (Figure 7d). Twenty-seven grains were analyzed (Th/U = 0.58–1.29). All zircons plot on or close to the Concordia pointing to the age of 247 ± 2 Ma (MSWD = 2.9; Figure 8d), which is interpreted to be the time of andesite emplacement.

4.4 | Nd–Hf isotopes

Seven analytical spots on the zircon grains/domains from the biotite-granite (Sample D0906) yielded initial $^{176}Hf/^{177}Hf$ values between 0.282753 and 0.282800 which are translated into $\varepsilon_{Hf}(t)$ values and two-stage model (T_{DM2}) ages ranging from +5.07 to +7.54 and from 775 to 898 Ma, respectively (Table 3). Eight analytical spots on zircon grains/domains from the granodiorite (Sample D0914) have $^{176}Hf/^{177}Hf$ values between 0.282747 and 0.282796 and corresponding $\varepsilon_{Hf}(t)$ values from +4.47 to +6.23 and T_{DM2} between 639 and 734 Ma. The whole-rock Nd isotope ratios yielded the initial $^{143}Nd/^{144}Nd$ of 0.512504 and $\varepsilon_{Nd}(t)$ value of 0.4, which corresponds to a T_{DM2} of 877 Ma.

FIGURE 7 Cathodoluminescence (CL) images of representative zircon crystals from the studied samples from the Middle Gobi Belt. White circles show individual analysis spots, corresponding U–Pb ages and red circles show an individual spot of Lu-Hf isotope and their $\varepsilon_{Hf}(t)$ values
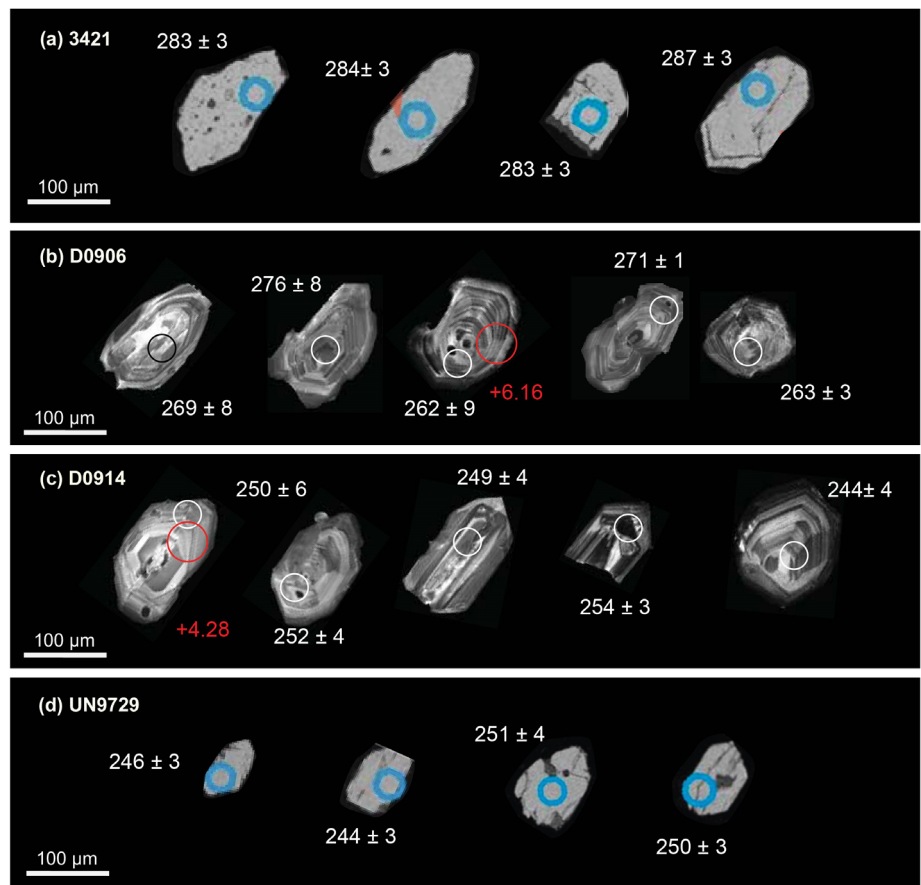
5 | DISCUSSION

5.1 | Timing of magmatism

The precise geochronological data are important to constrain the magmatic event and understand the tectonic evolution of the Middle Gobi Belt as they are rarely reported. Based on lithostratigraphic relationships and K–Ar ages, previous researchers considered that the Mandalgovi volcanoplutonic suite of the Middle Gobi Belt consists of the Neoproterozoic (Zaytsev & Luchitsky, 1979), early Cambrian, Devonian or early Permian (Gerel et al., 2019) formations. The state geological map shows the Mandalgovi biotite-granites as early Cambrian and Devonian in age (Zaytsev & Luchitsky, 1979). Our new zircon U–Pb data demonstrated Permian ages for gabbro at ∼285 Ma and for granite at ∼265 Ma. The ∼285 Ma gabbro is younger than the ∼316 Ma gabbro-diorite, whose emplacement has been related to subduction initiation in the MOO (Zhu et al., 2022), whereas the ∼265 Ma granite is coeval with the Permian S-type granites in NE Mongolia (Zhao et al., 2017).

The Precambrian age of the metamorphic basement (Figure 3) was constrained by relationships between so-called "early Cambrian" granites, as no radiogenic ages have been obtained so far. Absolute geochronological constraints of the alleged "Precambrian basement" metamorphic rocks are urgently needed in the near future.

In addition, our study reports the first Triassic zircon age of ∼250 Ma for the Mandalgovi pluton and the age of ∼247 Ma for andesites of the Middle Gobi Belt. These ages are slightly older than the age of the subduction-related granites in the Delgerkhaan area, Central Mongolia (220 Ma; Ganbat, Tsujimori, Miao, et al., 2021) and fit the age of the magmatic 'flare-up' in the NE China (Liu et al., 2018). Our data, combined with previous published data (e.g., Zhao et al., 2017; Zhu et al., 2016) indicate two periods of active magmatism in the Middle Gobi belt and in NE Mongolia: late Paleozoic and early Mesozoic.

5.2 | Petrogenesis and magma sources

5.2.1 | Early–Middle Permian magmatism

Gabbro, Gabbro-diorite
Gabbro, gabbro-diorite samples are mostly tholeiitic and characterized by low SiO_2 and total alkali, but high MgO, FeO^T, and CaO but enriched in LREE and LILE and depleted in HREEs and HFSEs. Those geochemical features are typical of arc magmas. Moreover, they are rich in hornblende, suggesting they have formed in a water-rich environment (e.g., Sisson et al., 1996).

In addition, those features can result from crustal contamination, since the average lithospheric mantle and continental crust are both

TABLE 2 LA-ICPMS U–Th–Pb analytical data for zircons of the studied samples from the Middle Gobi Belt

Sample name	Isotope ratios						Age						Th/U
	$^{207}Pb/^{235}U$	2σ	$^{206}Pb/^{238}U$	2σ	$^{207}Pb/^{206}Pb$	2σ	$^{235}U\text{-}^{207}Pb$	2σ	$^{238}U\text{-}^{206}Pb$	2σ	$^{207}Pb\text{-}^{206}Pb$	2σ	
3421-Gabbro													
PRB11	0.3249	0.001	0.0443	0.184	0.0532	0.001	286	4	279	4	339	36	0.37
PRB21	0.3576	0.009	0.0449	0.213	0.0577	0.002	310	6	283	3	518	56	0.54
PRB16	0.3256	0.005	0.0448	0.184	0.0527	0.001	286	4	283	3	316	36	0.39
PRB05	0.3198	0.005	0.0046	0.179	0.0518	0.001	282	5	287	3	276	36	0.01
PRB28[a]	0.3693	0.010	0.0095	0.221	0.0587	0.002	319	6	287	3	557	58	0.81
PRB24	0.3452	0.008	0.0080	0.208	0.0550	0.001	301	5	288	3	413	53	1.27
PRB02	0.3262	0.012	0.0115	0.240	0.0519	0.002	287	7	291	3	281	82	0.48
PRB25	0.3838	0.007	0.0074	0.192	0.0602	0.001	330	5	288	4	612	44	0.92
PRB19	0.3223	0.009	0.0085	0.210	0.0511	0.001	284	5	284	2	245	62	0.75
D0906-Biotite-granite													
D0906-2	0.31903	0.016	0.04262	0.001	0.05429	0.002	281.2	12.2	269.05	8.41	269.6	8.43	1.1
D0906-6	0.31848	0.017	0.04207	0.001	0.05491	0.002	280.7	13	265.65	8.41	266.11	8.44	0.8
D0906-7	0.30387	0.018	0.04382	0.001	0.05029	0.002	269.4	14	276.47	8.83	275.93	8.77	1.0
D0906-8	0.29395	0.017	0.04170	0.002	0.05112	0.002	261.7	13	263.36	9.65	263.18	9.59	0.9
D0906-9	0.30686	0.017	0.04181	0.002	0.05323	0.002	271.7	13.1	264.04	9.65	264.58	9.66	1.1
D0906-10	0.28987	0.016	0.04305	0.002	0.04883	0.002	258.5	12.3	271.71	9.89	269.23	9.69	1.0
D0906-12	0.29598	0.016	0.04151	0.002	0.05172	0.002	263.3	12.2	262.19	9.53	262.31	9.49	0.9
D0906-14	0.28405	0.019	0.04240	0.002	0.04859	0.003	253.9	15	267.69	9.96	266.31	9.85	0.9
D0906-18	0.29943	0.015	0.04197	0.002	0.05174	0.002	266	12	265.03	9.65	265.15	9.59	1.1
D0906-20	0.30614	0.018	0.04124	0.002	0.05384	0.002	271.2	13.9	260.51	9.6	261.02	9.62	0.7
D0906-24	0.28327	0.012	0.04133	0.001	0.04971	0.002	253.25	9.45	261.07	6.75	260.22	6.68	0.9
D0906-26	0.31008	0.014	0.04222	0.001	0.05326	0.002	274.2	11.2	266.58	6.99	266.91	6.99	0.7
D0906-27	0.31148	0.013	0.04199	0.001	0.05379	0.002	275.3	10	265.16	6.87	265.67	6.88	1.2
D0906-28	0.28250	0.017	0.04176	0.001	0.04906	0.003	252.6	13.3	263.73	7.12	263.15	7.08	0.8
D0914 Hornblende-granite													
D0914-1	0.27719	0.012	0.03968	0.001	0.05066	0.002	248.43	9.48	250.85	6.51	250.65	6.48	1.2
D0914-5	0.27261	0.012	0.04005	0.001	0.04937	0.002	244.78	9.19	253.14	6.51	252.28	6.45	0.9
D0914-7	0.27792	0.010	0.03957	0.001	0.05093	0.002	249.01	8.24	250.17	4.46	250.12	4.45	1.0
D0914-8	0.28394	0.010	0.03940	0.001	0.05226	0.002	253.78	7.94	249.11	4.4	249.27	4.4	0.9
D0914-9	0.26643	0.009	0.03870	0.001	0.04994	0.001	239.84	7.38	244.77	4.28	244.51	4.27	1.5
D0914-10	0.30477	0.011	0.03983	0.001	0.05549	0.002	270.12	8.61	251.78	4.46	251.9	4.48	1.3

TABLE 2 (Continued)

Sample name	Isotope ratios						Age						Th/U
	$^{207}Pb/^{235}U$	2σ	$^{206}Pb/^{238}U$	2σ	$^{207}Pb/^{206}Pb$	2σ	$^{235}U-^{207}Pb$	2σ	$^{238}U-^{206}Pb$	2σ	$^{207}Pb-^{206}Pb$	2σ	
D0914-14	0.29357	0.011	0.04023	0.001	0.05292	0.002	261.37	8.72	254.26	4.52	254.42	4.52	1.0
D0914-15	0.28971	0.011	0.03998	0.001	0.05256	0.002	258.33	8.5	252.71	4.46	252.84	4.46	1.1
D0914-20	0.31925	0.016	0.04086	0.002	0.05667	0.002	281.3	12.3	258.2	10.3	258.4	10.6	1.0
D0914-22	0.28861	0.014	0.04032	0.002	0.05191	0.001	257.5	11.3	254.8	10.2	255.4	10.2	1.2
D0914-24	0.27784	0.014	0.03875	0.002	0.05200	0.002	248.9	11.5	245.08	9.87	245.68	9.84	1.1
D0914-25	0.28179	0.015	0.03910	0.002	0.05226	0.002	252.1	12.1	247.25	9.99	247.84	9.97	1.0
D0914-29	0.29948	0.016	0.03921	0.002	0.05540	0.002	266	12.4	247.93	9.99	248.5	10.1	1.0
D0914-33	0.32260	0.017	0.04028	0.002	0.05808	0.002	283.9	13.4	254.6	10	253.8	10.2	0.9
D0914-34	0.28526	0.016	0.03980	0.002	0.05199	0.002	254.8	12.8	251.59	9.98	251.93	9.95	1.0
D0914-35	0.27142	0.014	0.03887	0.002	0.05064	0.002	243.8	11.3	245.82	9.68	245.46	9.57	1.3
UN9729-Andesite													
PRB12	0.27830	0.007	0.03820	0.000	0.05290	0.001	249	6	242	3	325	60	0.76
PRB28	0.27660	0.010	0.03840	0.001	0.05230	0.002	248	8	243	3	300	82	0.78
PRB23	0.27490	0.014	0.03850	0.001	0.05180	0.003	247	11	244	3	277	116	0.84
PRB10	0.41670	0.023	0.03990	0.001	0.07580	0.004	354	17	252	4	1089	111	0.81
PRB27	0.29330	0.010	0.03890	0.001	0.05470	0.002	261	8	246	3	400	78	0.78
PRB26	0.34880	0.018	0.03940	0.001	0.06430	0.003	304	13	249	4	750	106	0.97
PRB22	0.30310	0.014	0.03910	0.001	0.05630	0.003	269	11	247	3	464	102	0.92
PRB15	0.27900	0.008	0.03890	0.000	0.05210	0.002	250	6	246	3	287	65	0.65
PRB01	0.32100	0.014	0.03930	0.001	0.05930	0.003	283	11	249	3	578	93	1.19
PRB24	0.32520	0.014	0.03940	0.001	0.06000	0.003	286	10	249	3	602	91	0.69
PRB29	0.32360	0.014	0.03940	0.001	0.05970	0.003	285	11	249	3	592	94	0.81
PRB07	0.34010	0.017	0.03950	0.001	0.06240	0.003	297	13	250	4	689	104	0.78
PRB14	0.37890	0.017	0.03990	0.001	0.06900	0.003	326	13	252	3	898	92	0.78
PRB05	0.34430	0.012	0.03960	0.001	0.06310	0.002	300	9	251	3	710	77	0.71
PRB20	0.35130	0.013	0.03980	0.001	0.06420	0.003	306	10	251	3	747	80	0.78
PRB18	0.56640	0.036	0.04160	0.001	0.09890	0.006	456	23	263	5	1603	117	0.58
PRB08	0.29230	0.010	0.03930	0.001	0.05400	0.002	260	8	248	3	373	78	1.04
PRB04	0.34120	0.022	0.03970	0.001	0.06240	0.004	298	17	251	4	688	136	0.72
PRB21	0.29600	0.010	0.03930	0.001	0.05460	0.002	263	8	249	3	398	78	0.75
PRB13	0.35080	0.019	0.03980	0.001	0.06390	0.004	305	14	252	4	739	113	0.65
PRB03	0.30850	0.011	0.03950	0.001	0.05670	0.002	273	8	250	3	477	77	1.01

(Continues)

TABLE 2 (Continued)

Sample name	Isotope ratios						Age						Th/U
	$^{207}Pb/^{235}U$	2σ	$^{206}Pb/^{238}U$	2σ	$^{207}Pb/^{206}Pb$	2σ	^{235}U-^{207}Pb	2σ	^{238}U-^{206}Pb	2σ	^{207}Pb-^{206}Pb	2σ	
PRB02	0.28530	0.012	0.03930	0.002	0.05270	0.002	255	10	249	3	314	96	1.29
PRB11	0.30970	0.013	0.03960	0.001	0.05680	0.003	274	10	250	3	484	95	0.61
PRB09	0.31450	0.011	0.03960	0.001	0.05760	0.002	278	8	250	3	515	76	1.25
PRB17	0.29670	0.014	0.03950	0.001	0.05460	0.003	264	11	250	3	394	106	0.92
PRB16	0.29220	0.007	0.03950	0.000	0.05370	0.001	260	6	250	3	357	58	0.85
PRB06	0.28870	0.019	0.03990	0.001	0.05250	0.004	258	15	252	4	306	145	0.83

^aDiscordant data excluded from calculation. Spots in italic are excluded.

depleted in Nb and Ta relative to neighboring elements (Th, La) (Rudnick et al., 2003). However, significant crustal contamination leads not only to Nb–Ta depletion but also increases concentrations of Zr and Hf, giving rise to negative Nb–Ta anomalies and positive Zr–Hf anomalies in mantle-normalized trace element spidergrams (Figure 6b) (Zhao & Zhou, 2009). The Mandalgovi gabbro-diorites display troughs at Nb–Ta, and Zr, and peaks at Pb, which cannot be completely attributed to crustal contamination, but could indicate arc-derived magmatism.

Nb is commonly depleted in the lithospheric mantle relative to La, so low Nb/La ratios (<0.5) for mafic magmas suggest a lithospheric mantle source, and higher ratios (>1) indicate an OIB-like asthenospheric mantle source (Smith et al., 1999). The Nb/La ratios for the gabbro-diorites are between 0.1 and 0.3, that is, closer to the lithospheric mantle source.

Sahalyn gol rhyolite and biotite-granite

In the field, the Sahalyn gol rhyolite crops out near the ∼265 Ma biotite-granites (Figure 2) and probably was derived from similar levels in the crust. A state geological mapping report (Zaytsev & Luchitsky, 1979) mentions that rhyolites of the Sahalyn gol formation are cut by Mandalgovi granitoid (∼250 Ma). A felsic tuff layer of the Sahalyn gol formation carries *Cordaites* cf., *Ruflora* sp. nov floras of Kungurian age (281–273 Ma) (Baasan et al., 2022). Petrographically, the biotite granite and rhyolite share a similar mineral assemblage: plagioclase, quartz, biotite, and accessory titanite, apatite, opaque minerals, and zircon. These rocks have also similar whole-rock chemical features: both, rhyolite and granite, have high-K, high Al_2O_3, are enriched in LREEs, depleted in HFSEs and HREEs, and show similar spidergrams with Eu anomaly (Figures 5 and 6). We consider that the Sahalyn gol rhyolite coeval with the biotite-granite and discuss their petrogenetic origin together below.

The biotite-granite and Sahalyn gol rhyolite are characterized by high SiO_2, K, Rb, Pb, and low Na_2O, REE, and Sr, and peraluminous character in A/CNK versus A/NK plot (Figure 5d). Peraluminous, Si-rich granites can be produced by (1) partial melting of Al-rich metapelite and metagraywacke (Eyal et al., 2004; Healy et al., 2004; Patiño Douce, 1999); (2) partial melting of tonalite or granodiorite at pressures ≥8 kbar with restitic clinopyroxene (Patiño Douce, 1999); (3) mixing of the basaltic magma with terrigenous sediments. The negative Nb–Ti and P anomalies can be related to the fractionation of Ti-phases and apatite, respectively. We did not observe a wide range $\epsilon_{Hf}(t)$ and $\epsilon_{Nd}(t)$ values, nor abundance of the mafic microgranular enclaves within biotite-bearing granites, both being considered as indicators of magma mixing and source heterogeneity, do not support the mixing model. The Eu troughs in the REE spectra (Figure 6d) and the Sr negative trend in the Ba versus Sr and Sr versus Eu diagrams (Figure 9a,b) indicate fractionation of plagioclase. In the diagrams of $(Na_2O + K_2O)/(FeO^T + TiO_2)$ versus $(Na_2O + K_2O + FeO^T + MgO + TiO_2)$ and $Al_2O_3/(MgO + FeO^T)$ vs. $CaO/(MgO + FeO^T)$ diagrams indicate partial melting of a metagraywacke source for generating the biotite-granitic magma (Figure 10a,b). The Rb/Ba versus Rb/Sr ratios indicate that the source magma was from clay-poor melts (Figure 10c,d).

FIGURE 8 Concordia diagrams of zircons for samples from the Middle Gobi Belt, showing U–Pb isotope ratios. Light grayish ellipses indicate discordant data excluded from the calculation
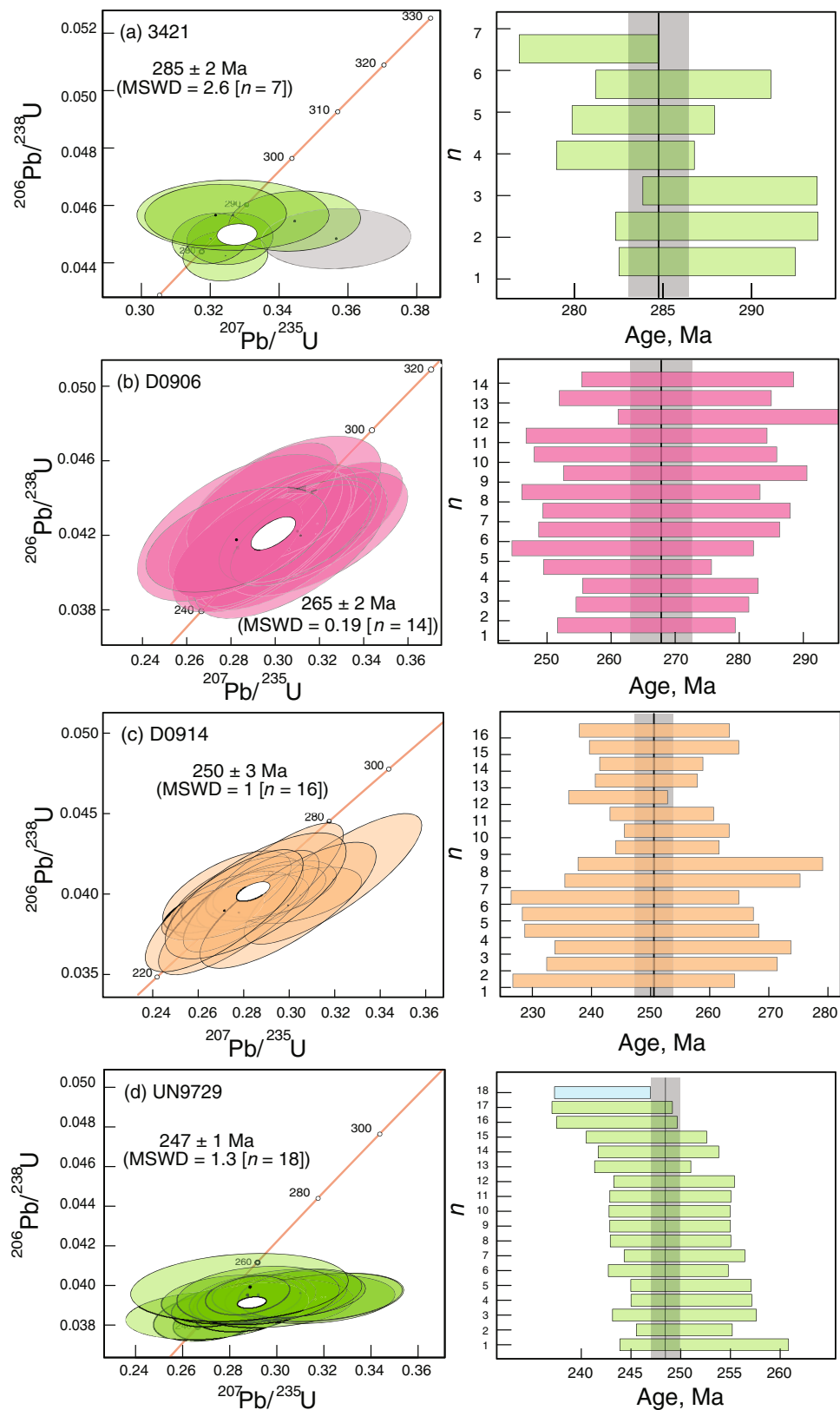
The positive $\epsilon_{Hf}(t)$ values may indicate the involvement of a mantle-derived component in the petrogenesis of these biotite-granites (Figure 11). The juvenile $\epsilon_{Hf}(t)$ isotopic signature may be associated with the emplacement of mantle-derived igneous rocks into supracrustal sedimentary units, which thus acquired juvenile isotopic characteristics (e.g., Healy et al., 2004). We assume that the primary magma of the Mandalgovi biotite-granite was derived through the melting of metagraywacke formed by the destruction of mantle-derived igneous rocks.

TABLE 3 Zircon Lu-Hf and whole-rock Sm-Nd isotope data of the studied samples from the Middle Gobi Belt.

Spot	Age, Ma	$^{176}Yb/^{177}Hf$	$^{176}Lu/^{177}Hf$	$^{176}Hf/^{177}Hf$	2 s	$\varepsilon_{Hf}(t)$	T_{DM}	T_{DMC} Lu/Hf = 0.015	$(^{176}Hf/^{177}Hf)i$	$^{176}Hf/^{177}Hf(DM)i$	$f_{Lu/Hf}$	2 s
D0914-Hornblende granodiorite												
7.1	249	0.020205	0.000720	0.282747	0.000020	4.47	711	994	0.282743	0.283070	−0.98	0.6904
8.1	253	0.028939	0.001043	0.282768	0.000020	5.15	687	950	0.282763	0.283071	−0.97	0.6957
10.1	251	0.018934	0.000679	0.282795	0.000020	6.21	642	883	0.282792	0.283070	−0.98	0.7096
11.1	239	0.023660	0.000881	0.282796	0.000026	5.97	644	889	0.282792	0.283078	−0.97	0.9200
24.1	248	0.021468	0.000783	0.282758	0.000023	4.78	695	970	0.282755	0.283074	−0.98	0.7974
25.1	252	0.028522	0.001020	0.282760	0.000023	4.84	697	968	0.282755	0.283073	−0.97	0.8254
29.1	266	0.017429	0.000632	0.282797	0.000023	6.23	639	880	0.282794	0.283072	−0.98	0.7990
31.1	268	0.020348	0.000745	0.282730	0.000022	4.28	734	1020	0.282727	0.283057	−0.98	0.7759
D0906-Biotie-granite												
1.1	281	0.039100	0.001305	0.282853	0.000025	7.54	570	775	0.282848	0.283091	−0.96	0.8850
6.1	280	0.021466	0.000780	0.282785	0.000023	6.16	658	898	0.282781	0.283059	−0.98	0.7979
7.1	269	0.030064	0.001016	0.282750	0.000024	5.07	711	974	0.282745	0.283053	−0.97	0.8604
9.1	271	0.024690	0.000834	0.282783	0.000024	6.04	662	905	0.282779	0.283060	−0.97	0.8364
10.1	258	0.022115	0.000793	0.282800	0.000022	6.75	637	863	0.282796	0.283057	−0.98	0.7653
11.1	263	0.026817	0.000898	0.282820	0.000023	6.31	611	850	0.282816	0.283095	−0.97	0.8222
13.1	253	0.030760	0.001074	0.282825	0.000025	7.51	607	812	0.282819	0.283059	−0.97	0.8887

Sample	Age, Ma	Sm, ppm	Nd, ppm	$^{147}Sm/^{144}Nd$	$^{143}Nd/^{144}Nd$	±2 s	$\varepsilon_{Nd}(0)$	$\varepsilon_{Nd}(t)$	$t_{Nd(DM)}$	$t_{Nd(C)}$
D0914	250	4.25	25.4	0.1011	0.512504	3	−2.6	0.4	877	1003

FIGURE 9 (a) Ba versus Sr diagram, (b) Sr versus Eu diagram showing mineral fractionation
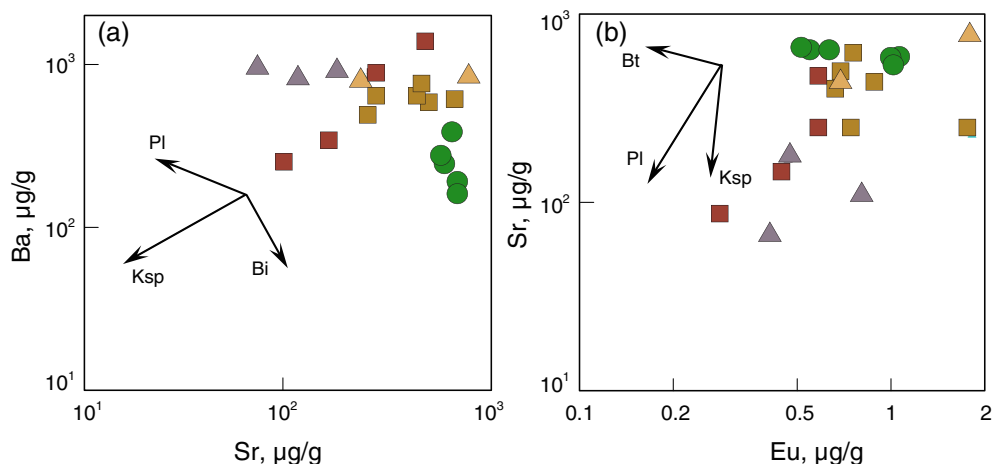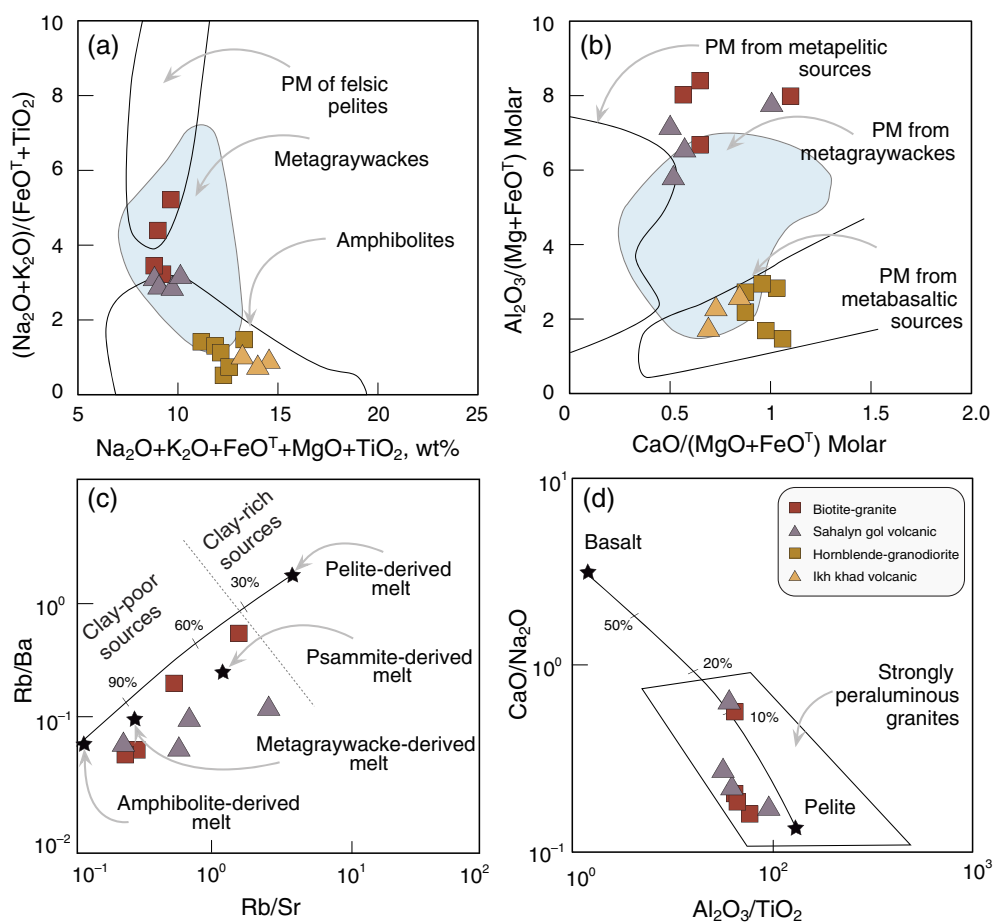

FIGURE 10 (a) $(Na_2O + K_2O)/(FeO^T + TiO_2)$ versus $Na_2O + K_2O + FeO^T + MgO + TiO_2$, wt% diagram, (b) molar $Al_2O_3/(Mg + FeO^T)$ versus molar $CaO/(MgO + FeO^T)$ for source determination, (c) Plots of Rb/Ba versus Rb/Sr, (d) CaO/Na_2O versus Al_2O_3/TiO_2 plots for source characteristics (Patiño Douce & Harris, 1998; Patiño Douce & Johnston, 1991)

5.3 | Triassic magmatism

5.3.1 | Hornblende-granite

The Mandalgovi hornblende-granite samples are Na-rich and classified as metaluminous granitoids (Figure 5a). In general, calc-alkaline metaluminous granites form by assimilation and fractional crystallization of mantle-derived basaltic sources, mixing of mafic magma with crust-derived felsic magma, or partial melting of juvenile mafic crust (e.g., Chappell & White, 2001; Clemens et al., 2011; Kemp et al.,

2007; Moyen et al., 2017). Metaluminous granites generated by magma mixing typically carry abundant mafic enclaves and have a variable chemical composition (e.g., Chappell, 1996), which is not observed in our samples. Na-rich ($Na_2O/K_2O > 1$), high-Al_2O_3 melts with intermediate to silicic compositions may be produced by ~20%–40%, leaving a granulite residue and/or garnet granulite to eclogite residues (Rapp, 1995; Rapp & Watson, 1995). However, unlike the biotite-granites, show no notable trends of fractionation (Figure 9a,b), supporting the partial melting scenario. The Mandalgovi hornblende-granitoids have low K and Th; and are dominated by intermediate
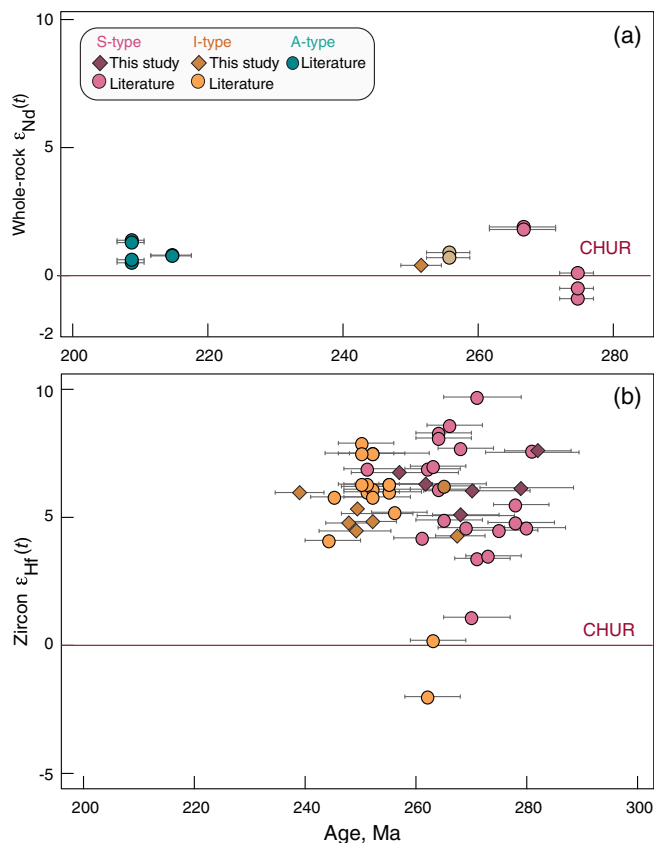
FIGURE 11 (a) Correlations between whole-rock $\varepsilon_{Nd}(t)$ and zircon concordant ages. (b) Correlations between $\varepsilon_{Hf}(t)$ and U–Pb ages of zircons for the studied samples from the Middle Gobi Belt. Compared data are from Zhu et al., 2016; Zhao et al., 2017

compositions, which are consistent with those of experimental melts derived by the dehydration melting of metabasalts or amphibolite (Figures 10a,b). Therefore, we think that the Mandalgovi hornblende-granites formed by the partial melting of the mafic lower crust. They are enriched in LILE (e.g., Rb, Ba) and depleted in Nb, Ta, and Ti, indicating crustal contribution (e.g., Bonin, 2004). The $\varepsilon_{Hf}(t)$ values of zircons and positive $\varepsilon_{Nd}(t)$ value indicate that the primary magmas for these units originated by partial melting of juvenile material. The presence of the zircon grains with negative $\varepsilon_{Hf}(t)$ values reported in the literature (Figure 11; Zhao et al., 2017) suggests that the magma was contaminated with wall rocks.

The Ikh khad dacitic samples exhibit high SiO_2, low MgO, Mg#, and Ni values, indicating that their precursor magma was unlikely derived from the partial melting of mantle rocks (e.g., Rudnick & Gao, 2013). The following mechanisms for the generation of felsic volcanics with such geochemical features are possible: (1) extensive and fractional crystallization of a mantle-derived basaltic primary magma (Charlier et al., 2007; Davidson et al., 2007); (2) magma mixing between basaltic magmas and felsic magmas (Kemp et al., 2007); (3) partial melting of a mafic to intermediate igneous source (Gillis, 2008). We think that the fractional crystallization from the basaltic magma model is not applicable to dacite, because these processes mostly result in continuous compositional trends, which are

not observed in our case (Figure 4b), and we see no mafic end members. The concentrations of major elements (e.g., MgO) do not correlate linearly with those of SiO_2 (not shown), excluding magma mixing and fractional crystallization (e.g., Patiño Douce, 1999). Therefore, we propose that the Ikh khad volcanic was likely derived by the partial melting of mafic to intermediate igneous sources. Their Na-rich character may indicate derivation from a basaltic source, such as oceanic crust or juvenile continental crust (Rapp & Watson, 1995; Sisson et al., 2005).

5.4 | Tectonic settings and implication

The Mandalgovi suite of the Middle Gobi Belt hosts spatially and temporally associated with the Permian gabbro, gabbro-diorite; peraluminous biotite-granite and rhyolites; early Triassic metaluminous hornblende-granodiorite, and felsic–intermediate volcanics.

The geochemical and isotope compositions of the igneous rocks of the Middle Gobi Belt suggest the following tectonic settings of their emplacement. In tectonic discrimination diagrams, the gabbro and gabbro-diorite samples are plotting on the active continental margin and island arc fields (Figures 12a and 13a). Their geochemical composition shows that they have formed by metasomatism of the lithospheric mantle (see Section 5.2.1). Together we propose that the early Permian gabbro and gabbro-diorite formed in a supra-subduction setting by metasomatism of the lithospheric mantle at ~295 Ma (Figure 14a).

The formation of peraluminous granites is generally attributed to collisional and/or post-collisional settings (Barbarin, 1996, 1999; Chappell & White, 2001). The small amount of peraluminous granites and the absence of detachment fault zones, gneiss domes, or metamorphic core-complexes, usually associated with the post-collisional granites makes a post-collisional setting rather unlikely (Figure 3). The abundant subduction-related magmatic complexes of the Central Mongolia–Erguna blocks formed during a period from the early Permian to the late Triassic (e.g., Ganbat, Tsujimori, Miao, et al., 2021; Zhao et al., 2017; Zhu et al., 2022). The primitive-mantle normalized patterns of the Permian peraluminous granite and Sahalyn gol rhyolite show negative anomalies at Nb, Ta, and Ti (Figure 6), which are, in turn, typical of subduction-related igneous rocks (e.g., Stern, 2002). In the tectonic discrimination diagrams (Pearce et al., 1984), these rocks plot in the field of volcanic arc (Figure 12c,d). We conclude that the peraluminous granite and the Sahalyn gol rhyolite recorded subduction component, either in a back-arc extension (Collins & Richards, 2008) or anatexis of forearc sediments (Clemens et al., 2017; Lytwyn et al., 2000). The back-arc extension model, for example, is proposed for the S-type granites of the New England orogen of the Circum-Pacific (Collins et al., 2020; Collins & Richards, 2008). This model suggests that back-arc extension is induced by repeated subduction zone retreat resulting in the melting of the sediment-dominated basin by hot basaltic magma intruded into the thinned back-arc crust. Such a setting requires a pre-history of subduction, to provide crustal thickening before the biotite-granite formed when the arc relocated below the thickened metasedimentary crust, whereas hornblende-

FIGURE 12 (a) MgO–Al$_2$O$_3$–FeO^T ternary diagram for tectonic discrimination of mafic rocks from the Middle Gobi Belt (Pearce et al., 1977); (b) Ba versus Zr tectonic discrimination diagram of mafic rocks from the Middle Gobi Belt (Shervais, 1982)
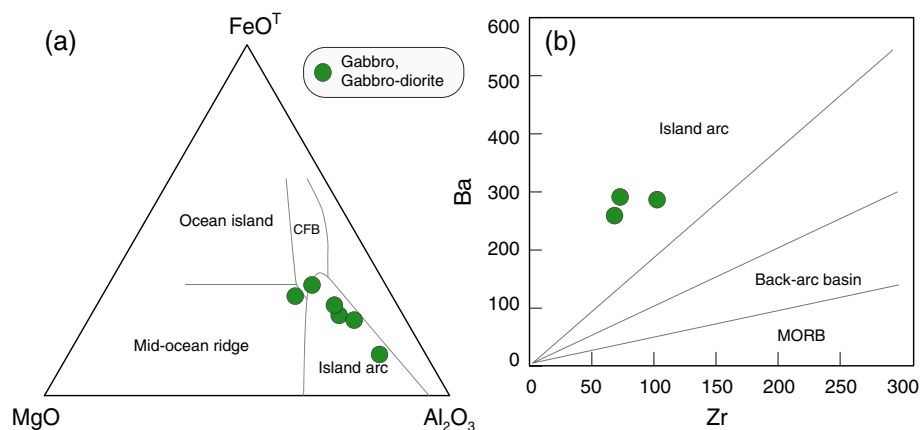

FIGURE 13 (a) Tectonic discrimination diagrams for the studied samples from the Middle Gobi Belt: (a) Th/Yb versus Ta/Yb (Pearce, 2008); (b) Th/Ta versus Yb (Schandl and Gorton, 2002) (c) Rb versus Ta + Yb (Pearce et al., 1984); (d) Hf–Rb/30–3*Ta (Harris et al., 1986). Syn-COLG, syn-collision granite; VAG, volcanic arc granite; WPG, within plate granite; Post-COLG, post-collisional granite; ACM, active continental margin; DM, depleted mantle; EM, enriched mantle
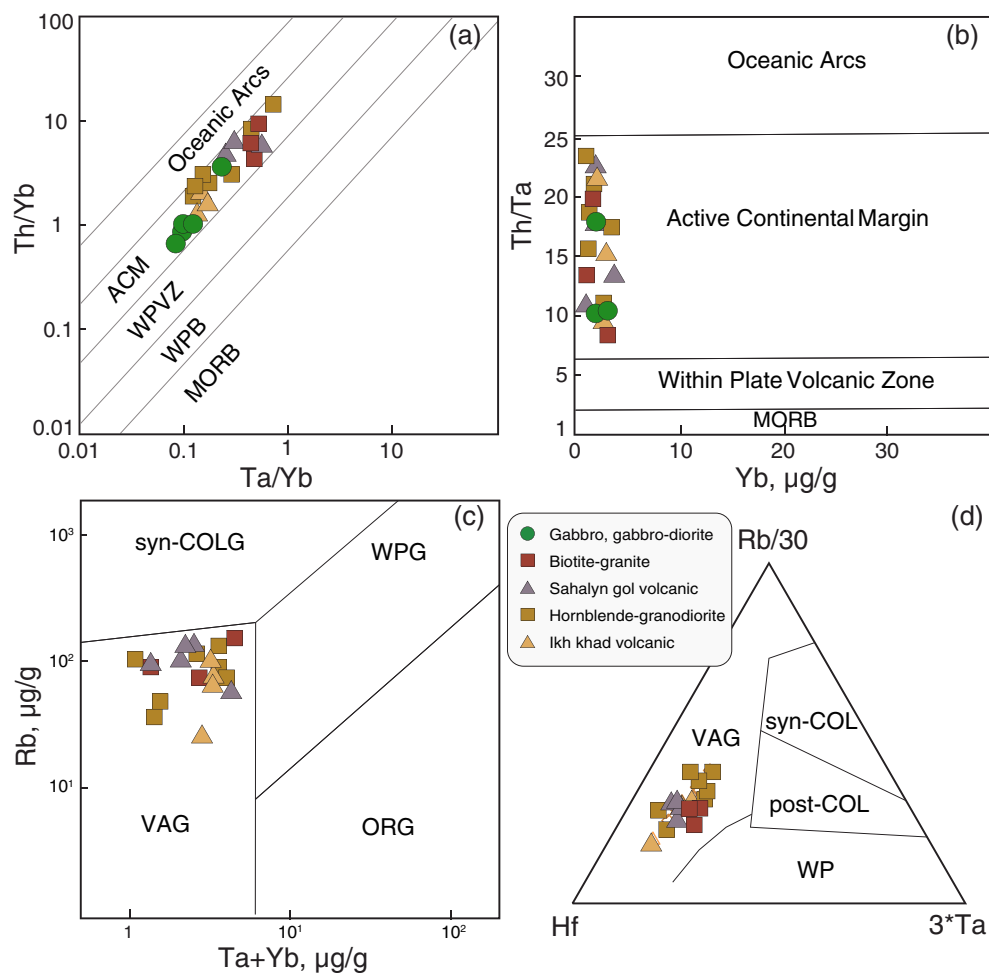
granodiorite formed as the arc moved outboard, so their position became inter-arc rift or proximal back-arc (Collins & Richards, 2008). This scenario was applied to the Permian S-type granitoids in NE Mongolia (Zhao et al., 2017), and explains well the formation of the Middle Gobi peraluminous granites in Permian time. The positive zircon $\varepsilon_{Hf}(t)$ values and whole-rock $\varepsilon_{Nd}(t)$ isotopic values (Figure 11a,b), plus the absence of strong peraluminous minerals (e.g., cordierite, garnet), in peraluminous samples, make them distinct from classical S-type granites (collision-related granites) (Figure 12a,b). Comparison

with the samples from the Middle Gobi Belt and the NE Mongolia shows that during 265 Ma, magmatism experienced stronger juvenile addition (Figure 11a,b), possibly related to the rifting. The juvenile Hf and Nd isotopic characters also are typical of greywackes formed by the destruction of juvenile igneous rocks formed in a supra-subduction setting (Safonova, 2017; Safonova et al., 2021). Therefore, we suggest that the peraluminous granites may have formed by melting of the arc-related volcanogenic sedimentary in the inter-arc rift setting (Healy et al., 2004; Jeon et al., 2012).
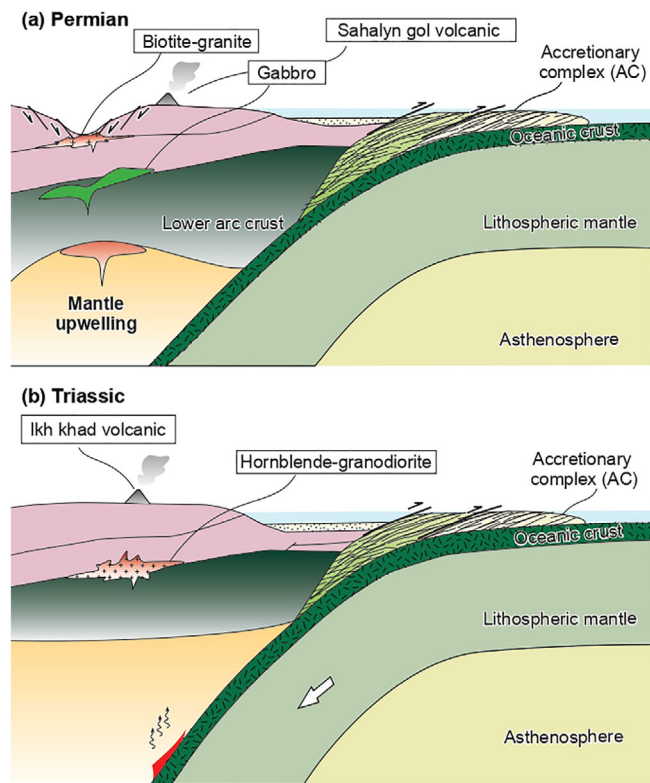
FIGURE 14 Tectonic model for the studied samples from the Middle Gobi Belt. (a) Cross-section depicting a mafic intrusion formed by the oceanic subduction of the MOO. Biotite-granite and Sahalyn Gol volcanic rock emplaced by intermittent extension during the subduction during the late Permian. (b) Hornblende-granodiorite and Ikh khad volcanic are forming during the continuous subduction of the MOO lithosphere during the Triassic

As discussed above, the Triassic hornblende-granite and Ikh khad dacite are derived from juvenile mafic components will crustal contribution (Section 5.3). Based on their concentration on the active continental margin and volcanic arc setting, we consider that the Triassic hornblende-granites and felsic–intermediate volcanics formed in a supra-subduction setting. Their neutral to positive $\varepsilon_{Hf}(t)$ (+0.4 to +7.5) and $\varepsilon_{Nd}(t)$ (0.4) characteristics and the T_{DM2} of 775–1019 Ma (Table 3) suggest the generation of primary magmas by the partial melting of a relatively depleted juvenile lower crust or depleted mantle source, implying that the crustal development occurred on the mature arc along the Andean-type active continental margin.

Ascertaining the tectonic setting of the Permian–Triassic igneous rocks in the Middle Gobi Belt is important in the context of refining our understanding of the tectonic evolution of the MOO.

The subduction of the MOO beneath the Central Mongolia microcontinent was recorded by the Adaatsag and Khukh Davaa ophiolites (Figures 1 and 2; Tomurtogoo et al., 2005; Zhu et al., 2022), which resulted in formation of the Carboniferous–Permian subduction-related magmatic complexes of the Middle Gobi Belt (Zhu et al., 2022), NE Mongolia (Zhao et al., 2017) and Erguna Belt (Liu et al.,, 2018). The study of these magmatic rocks is critical to

reconstructing the tectonic evolution of the MOO. The Carboniferous–Permian magmatic belts at the southern side of the Mongol–Okhotsk suture belt (Figure 1) formed at an Andean-type active continental margin (Figure 2; Tomurtogoo et al., 2005; Zhu et al., 2016; Zhao et al., 2017; Ganbat, Tsujimori, Miao, et al., 2021; Zhu et al., 2022).

The Permian–Triassic magmatism of the Middle Gobi was triggered by the continuous southward subduction of the Mongol–Okhotsk Ocean. The magmatic spatial and temporal distribution show that the context is that Mongol–Okhotsk oceanic subduction was still taking place in the early Mesozoic (Figure 2). The late Paleozoic–Mesozoic magmatism in Central and NE Mongolia and NE China indicate that the southward subduction of the MOO crust beneath the Central Mongolia–Erguna microcontinent started in the Carboniferous (Figure 13) and the intensive subduction-related magmatism occurred during the Permian–Triassic (Ganbat, Tsujimori, Miao, et al., 2021; Liu & Zhao, 2018; Tang et al., 2016; Zhao et al., 2017; Zhu et al., 2022). The new radiogenic ages obtained from the magmatic formations emplaced the southern margin of the Mongol–Okhotsk suture zone show no significant differences between the ages of the subduction-related magmatic complexes extended from west to east along the Mongol–Okhotsk suture belt and therefore suggest that the MOO was suturing and closing coherently, i.e. not in a scissor-like pattern during the Permian time.

6 | CONCLUSIONS

Based on the obtained results we draw the following conclusions:

1. The volcanoplutonic suite in the Middle Gobi Belt consists of Mandalgovi biotite-granite and hornblende-granodiorite, gabbro-diorite, and gabbro; and Sahalyn gol rhyolite, and Ikh khad felsic–intermediate volcanics.
2. The Mandalgovi gabbro and gabbro-diorite formed ~285 Ma, after partial melting of a metasomatized lithospheric mantle source in a supra-subduction setting.
3. The ~265 Ma Mandalgovi biotite-granite is the consequence of partial melting from metagraywackes, but was the primary magma originated from the mantle-derived juvenile source. The intermittent inter-arc extension during the subduction hiatus possibly was a geodynamic process to give access to the upwelling of mantle-derived magma and crustal melting along the active continental margin.
4. The Mandalgovi hornblende-granodiorite yielded a crystallization age of ~250 Ma and resulted from the partial melting of a mafic source. Ikh khad andesite emplaced at ~247 Ma. They were formed in a volcanic arc setting.
5. The Middle Gobi Belt may include active continental margin products, during the subduction of the Mongol–Okhotsk Oceanic lithosphere. The subduction-related magmatism along the southern margin do not show a systematic trend, implying that the Mongol–

Okhotsk Ocean possibly was not closed in a scissor-like pattern during the Permian.

CONFLICT OF INTEREST

The authors declare no conflict of interest.

ORCID

Ariuntsetseg Ganbat https://orcid.org/0000-0003-2464-4161
Tatsuki Tsujimori https://orcid.org/0000-0001-9202-7312
Laicheng Miao https://orcid.org/0000-0001-6296-4444
Inna Safonova https://orcid.org/0000-0002-0909-2330
Daniel Pastor-Galán https://orcid.org/0000-0002-0226-2739
Chimedtseren Anaad https://orcid.org/0000-0001-7878-0738
Shogo Aoki https://orcid.org/0000-0001-5093-1346
Kazumasa Aoki https://orcid.org/0000-0001-7645-6766

REFERENCES

Armstrong, R. L. (1981). Radiogenic isotopes: The case for crustal recycling on a near-steady-state no-continental-growth Earth. *Philosophical Transactions of the Royal Society of London. Series A, Mathematical and Physical Sciences*, 301(1461), 443–472.

Arzhannikova, A. V., Demonterova, E. I., Jolivet, M., Mikheeva, E. A., Ivanov, A. V., Arzhannikov, S. G., & Kamenetsky, V. S. (2022). Segmental closure of the Mongol-Okhotsk Ocean: Insight from detrital geochronology in the East Transbaikalia Basin. *Geoscience Frontiers*, 13(1), 101254.

Baasan, B., Munkhnasan, Ch., Odbayar, B., Mungunshagai, S., Dagva, B., Khishigbold, O., Budtsolmon, B., Dulguun, B., Sukhbaatar, D., & Lkhagvamegzerdagva, B. (2022). Report of the State Geological Map "Shuteen Ulaan Uul" 1:50 000 (in Mongolian).

Badarch, G., Cunningham, W. D., & Windley, B. F. (2002). A new terrane subdivision for Mongolia: Implications for the Phanerozoic crustal growth of Central Asia. *Journal of Asian Earth Sciences*, 21(1), 87–110.

Barbarin, B. (1996). Genesis of the two main types of peraluminous granitoids. *Geology*, 24(4), 295–298.

Barbarin, B. (1999). A review of the relationships between granitoid types, their origins and their geodynamic environments. *Lithos*, 46(3), 605–626.

Batsaikhan, U., Noriyoshi, T., Anaad, C., & Bayaraa, B. (2018). Petrochemical characteristics of late Paleozoic magmatic rocks of the Mandakh area, southeast Mongolia. *Mongolian Geoscientist*, 47, 5–21.

Belousova, E. A., Kostitsyn, Y. A., Griffin, W. L., Begg, G. C., O'Reilly, S. Y., & Pearson, N. J. (2010). The growth of the continental crust: Constraints from zircon Hf-isotope data. *Lithos*, 119(3–4), 457–466.

Bonin, B. (2004). Do coeval mafic and felsic magmas in post-collisional to within-plate regimes necessarily imply two contrasting, mantle and crustal, sources? A review. *Lithos*, 78(1-2), 1–24.

Bouvier, A., Vervoort, J. D., & Patchett, P. J. (2008). The Lu–Hf and Sm–Nd isotopic composition of CHUR: Constraints from unequilibrated chondrites and implications for the bulk composition of terrestrial planets. *Earth and Planetary Science Letters*, 273(1–2), 48–57.

Buslov, M. M., Saphonova, I. Y., Watanabe, T., Obut, O. T., Fujiwara, Y., Iwata, K., & Kazansky, A. Y. (2001). Evolution of the Paleo-Asian Ocean (Altai-Sayan Region, Central Asia) and collision of possible Gondwana-derived terranes with the southern marginal part of the Siberian continent. *Geosciences Journal*, 5(3), 203–224.

Bussien, D., Gombojav, N., Winkler, W., & Von Quadt, A. (2011). The Mongol–Okhotsk Belt in Mongolia—An appraisal of the geodynamic development by the study of sandstone provenance and detrital zircons. *Tectonophysics*, 510(1–2), 132–150.

Chappell, B. W. (1996). Magma mixing and the production of compositional variation within granite suites: Evidence from the granites of southeastern Australia. *Journal of Petrology*, 37(3), 449–470.

Chappell, B. W., & White, A. J. (2001). Two contrasting granite types: 25 years later. *Australian Journal of Earth Sciences*, 48(4), 489–499.

Charlier, B. L. A., Bachmann, O., Davidson, J. P., Dungan, M. A., & Morgan, D. J. (2007). The upper crustal evolution of a large silicic magma body: Evidence from crystal-scale Rb–Sr isotopic heterogeneities in the Fish Canyon magmatic system, Colorado. *Journal of Petrology*, 48(10), 1875–1894.

Clemens, J. D., Buick, I. S., & Kisters, A. F. M. (2017). The Donkerhuk batholith, Namibia: A giant S-type granite emplaced in the mid crust, in a fore-arc setting. *Journal of the Geological Society*, 174(1), 157–169.

Clemens, J. D., Stevens, G., & Farina, F. (2011). The enigmatic sources of I-type granites: The peritectic connexion. *Lithos*, 126(3–4), 174–181.

Cogné, J. P., Kravchinsky, V. A., Halim, N., & Hankard, F. (2005). Late Jurassic-Early Cretaceous closure of the Mongol-Okhotsk Ocean demonstrated by new Mesozoic palaeomagnetic results from the Trans-Baikal area (SE Siberia). *Geophysical Journal International*, 163(2), 813–832.

Collins, W. J., Huang, H. Q., Bowden, P., & Kemp, A. I. S. (2020). Repeated S–I–A-type granite trilogy in the Lachlan Orogen and geochemical contrasts with A-type granites in Nigeria: Implications for petrogenesis and tectonic discrimination. *Geological Society, London, Special Publications*, 491(1), 53–76.

Collins, W. J., & Richards, S. W. (2008). Geodynamic significance of S-type granites in circum-Pacific orogens. *Geology*, 36(7), 559–562.

Dagva-Ochir, L., Oyunchimeg, T. U., Enkhdalai, B., Safonova, I., Li, H., Otgonbaatar, D., Tamehe, S., & Sharav, D. (2020). Middle paleozoic intermediate-mafic rocks of the Tsoroidog Uul'accretionary complex, Central Mongolia: Petrogenesis and tectonic implications. *Lithos*, 376, 105795.

Davidson, J., Turner, S., Handley, H., Macpherson, C., & Dosseto, A. (2007). Amphibole "sponge" in arc crust? *Geology*, 35(9), 787–790.

Demoux, A., Kröner, A., Liu, D., & Badarch, G. (2009). Precambrian crystalline basement in southern Mongolia as revealed by SHRIMP zircon dating. *International Journal of Earth Sciences*, 98(6), 1365–1380.

Dobretsov, N. L., Berzin, N. A., & Buslov, M. M. (1995). Opening and tectonic evolution of the Paleo-Asian Ocean. *International Geology Review*, 37(4), 335–360.

Eyal, M., Litvinovsky, B. A., Katzir, Y., & Zanvilevich, A. N. (2004). The Pan-African high-K calc-alkaline peraluminous Elat granite from southern Israel: Geology, geochemistry and petrogenesis. *Journal of African Earth Sciences*, 40(3–4), 115–136.

Ganbat, A., Tsujimori, T., Boniface, N., Pastor-Galán, D., Aoki, S., & Aoki, K. (2021). Crustal evolution of the paleoproterozoic Ubendian Belt (SW Tanzania) western margin: A Central African Shield amalgamation tale. *Gondwana Research*, 91, 286–306.

Ganbat, A., Tsujimori, T., Miao, L., Safonova, I., Pastor-Galán, D., Anaad, C., Baatar, M., & Savinskiy, I. (2021). Late Paleozoic–Early Mesozoic granitoids in the Khangay-Khentey basin, Central Mongolia: Implication for the tectonic evolution of the Mongol-Okhotsk Ocean margin. *Lithos*, 106455.

Gerel, O., Batkhishig, B., Munkhtsengel, B., & Javkhlan, O. (2019). Geochemistry and geochronology of Mandalgovi Complex. *Mongolian Geoscientist (In Mongolian with English abstract), 48*, 21–26.

Gillis, K. M. (2008). The roof of an axial magma chamber: A hornfelsic heat exchanger. *Geology, 36*(4), 299–302.

Goldstein, S. J., & Jacobsen, S. B. (1988). Nd and Sr isotopic systematics of river water suspended material: Implications for crustal evolution. *Earth and Planetary Science Letters, 87*(3), 249–265.

Harris, N. B., Pearce, J. A., & Tindle, A. G. (1986). Geochemical characteristics of collision-zone magmatism. *Geological Society, London, Special Publications, 19*(1), 67–81.

Hawkesworth, C. J., Dhuime, B., Pietranik, A. B., Cawood, P. A., Kemp, A. I., & Storey, C. D. (2010). The generation and evolution of the continental crust. *Journal of the Geological Society, 167*(2), 229–248.

Healy, B., Collins, W. J., & Richards, S. W. (2004). A hybrid origin for Lachlan S-type granites: The Murrumbidgee Batholith example. *Lithos, 78*(1–2), 197–216.

Irvine, T. N., & Baragar, W. R. A. (1971). A guide to the chemical classification of the common volcanic rocks. *Canadian Journal of Earth Sciences, 8*(5), 523–548.

Jacobsen, S. B., & Wasserburg, G. J. (1984). Sm-Nd isotopic evolution of chondrites and achondrites, II. *Earth and Planetary Science Letters, 67*(2), 137–150.

Jahn, B. M. (2004). The Central Asian Orogenic Belt and growth of the continental crust in the Phanerozoic. *Geological Society, London, Special Publications, 226*(1), 73–100.

Jahn, B. M., Litvinovsky, B. A., Zanvilevich, A. N., & Reichow, M. (2009). Peralkaline granitoid magmatism in the Mongolian–Transbaikalian Belt: Evolution, petrogenesis and tectonic significance. *Lithos, 113*(3–4), 521–539.

Jahn, B. M., Wu, F., & Chen, B. (2000). Massive granitoid generation in Central Asia: Nd isotope evidence and implication for continental growth in the Phanerozoic. *Episodes, 23*(2), 82–92.

Jeon, H., Williams, I. S., & Chappell, B. W. (2012). Magma to mud to magma: Rapid crustal recycling by Permian granite magmatism near the eastern Gondwana margin. *Earth and Planetary Science Letters, 319*, 104–117.

Jochum, K. P., Weis, U., Stoll, B., Kuzmin, D., Yang, Q., Raczek, I., & Enzweiler, J. (2011). Determination of reference values for NIST SRM 610–617 glasses following ISO guidelines. *Geostandards and Geoanalytical, 35*, 397–429.

Kelty, T. K., Yin, A., Dash, B., Gehrels, G. E., & Ribeiro, A. E. (2008). Detrital-zircon geochronology of paleozoic sedimentary rocks in the Hangay–Hentey basin, north-central Mongolia: Implications for the tectonic evolution of the Mongol–Okhotsk Ocean in central Asia. *Tectonophysics, 451*(1–4), 290–311.

Kemp, A. I. S., Hawkesworth, C. J., Foster, G. L., Paterson, B. A., Woodhead, J. D., Hergt, J. M., Gray, C., & Whitehouse, M. J. (2007). Magmatic and crustal differentiation history of granitic rocks from Hf-O isotopes in zircon. *Science, 315*(5814), 980–983.

Khanchuk, A. I., Didenko, A. N., Popeko, L. I., Sorokin, A. A., & Shevchenko, B. F. (2015). Structure and evolution of the Mongol-Okhotsk orogenic belt, 211. The Central Asian Orogenic Belt. Geology, Evolution, Tectonics, and Models. Kröner. A. *Borntraeger Science Publishers.*

Kravchinsky, V. A., Cogné, J. P., Harbert, W. P., & Kuzmin, M. I. (2002). Evolution of the Mongol-Okhotsk Ocean as constrained by new palaeomagnetic data from the Mongol-Okhotsk suture zone, Siberia. *Geophysical Journal International, 148*(1), 34–57.

Kröner, A., Kovach, V., Alexeiev, D., Wang, K. L., Wong, J., Degtyarev, K., & Kozakov, I. (2017). No excessive crustal growth in the Central Asian Orogenic Belt: Further evidence from field relationships and isotopic data. *Gondwana Research, 50*, 135–166.

Kröner, A., Kovach, V., Belousova, E., Hegner, E., Armstrong, R., Dolgopolova, A., & Rytsk, E. (2014). Reassessment of continental growth during the accretionary history of the Central Asian Orogenic Belt. *Gondwana Research, 25*(1), 103–125.

Kröner, A., Lehmann, J., Schulmann, K., Demoux, A., Lexa, O., Tomurhuu, D., Štípská, P., Liu, D., & Wingate, M. T. (2010). Lithostratigraphic and geochronological constraints on the evolution of the Central Asian Orogenic Belt in SW Mongolia: Early Paleozoic rifting followed by late Paleozoic accretion. *American Journal of Science, 310*(7), 523–574.

Le Bas, M. J., Rex, D. C., & Stillman, C. J. (1986). The early magmatic chronology of Fuerteventura, Canary Islands. *Geological Magazine, 123*(3), 287–298.

Li, Y., Xu, W. L., Wang, F., Tang, J., Zhao, S., & Guo, P. (2017). Geochronology and geochemistry of late Paleozoic–early Mesozoic igneous rocks of the Erguna Massif, NE China: Implications for the early evolution of the Mongol–Okhotsk tectonic regime. *Journal of Asian Earth Sciences, 144*, 205–224.

Liu, H., Li, Y., He, H., Huangfu, P., & Liu, Y. (2018). Two-phase southward subduction of the Mongol-Okhotsk oceanic plate constrained by Permian-Jurassic granitoids in the Erguna and Xing'an massifs (NE China). *Lithos, 304*, 347–361.

Liu, H., & Zhao, J. H. (2018). Neoproterozoic peraluminous granitoids in the Jiangnan Fold Belt: Implications for lithospheric differentiation and crustal growth. *Precambrian Research, 309*, 152–165.

Lytwyn, J., Lockhart, S., Casey, J., & Kusky, T. (2000). Geochemistry of near-trench intrusives associated with ridge subduction, Seldovia quadrangle, southern Alaska. *Journal of Geophysical Research: Solid Earth, 105*(B12), 27957–27978.

Machowiak, K., Stawikowski, W., & Achramowicz, S. (2012). Late Triassic 40Ar-39Ar ages of the Baga-Gazryn Chuluu granites (Central Mongolia). *Journal of Geosciences, 57*(3), 173–188.

Maniar, P. D., & Piccoli, P. M. (1989). Tectonic discrimination of granitoids. *Geological Society of America Bulletin, 101*(5), 635–643.

Metelkin, D. V., Vernikovsky, V. A., Kazansky, A. Y., & Wingate, M. T. (2010). Late Mesozoic tectonics of Central Asia based on paleomagnetic evidence. *Gondwana Research, 18*(2–3), 400–419.

Miao, L., Zhu, M., Liu, C., Baatar, M., Anaad, C., Yang, S., & Li, X. (2020). Detrital-Zircon age spectra of neoproterozoic-paleozoic sedimentary rocks from the Ereendavaa Terrane in NE Mongolia: Implications for the Early-Stage Evolution of the Ereendavaa Terrane and the Mongol-Okhotsk Ocean. *Minerals, 10*(9), 742.

Moyen, J. F., Laurent, O., Chelle-Michou, C., Couzinié, S., Vanderhaeghe, O., Zeh, A., Villaros, A., & Gardien, V. (2017). Collision vs. subduction-related magmatism: Two contrasting ways of granite formation and implications for crustal growth. *Lithos, 277*, 154–177.

Parfenov, L. M., Popeko, L. I., & Tomurtogoo, O. (2001). Problems of tectonics of the Mongol-Okhotsk orogenic belt. *Geology of the Pacific Ocean, 16*(5), 797–830.

Patiño Douce, A. E. (1999). What do experiments tell us about the relative contributions of crust and mantle to the origin of granitic magmas? *Geological Society, London, Special Publications, 168*(1), 55–75.

Patiño Douce, A. E., & Harris, N. (1998). Experimental constraints on Himalayan anatexis. *Journal of Petrology, 39*(4), 689–710.

Patiño Douce, A. E., & Johnston, A. D. (1991). Phase equilibria and melt productivity in the pelitic system: Implications for the origin of peraluminous granitoids and aluminous granulites. *Contributions to Mineralogy and Petrology, 107*(2), 202–218.

Pearce, J. A. (2008). Geochemical fingerprinting of oceanic basalts with applications to ophiolite classification and the search for Archean oceanic crust. *Lithos, 100*(1-4), 14–48.

Pearce, J. A., Harris, N. B., & Tindle, A. G. (1984). Trace element discrimination diagrams for the tectonic interpretation of granitic rocks. *Journal of Petrology, 25*(4), 956–983.

Pearce, T. H., Gorman, B. E., & Birkett, T. C. (1977). The relationship between major element chemistry and tectonic environment of basic and intermediate volcanic rocks. *Earth and Planetary Science Letters, 36*(1), 121–132.

Peccerillo, A., & Taylor, S. R. (1976). Geochemistry of Eocene calc-alkaline volcanic rocks from the Kastamonu area, northern Turkey. *Contributions to Mineralogy and Petrology*, 58(1), 63–81.

Rapp, R. P. (1995). Amphibole-out phase boundary in partially melted metabasalt, its control over liquid fraction and composition, and source permeability. *Journal of Geophysical Research: Solid Earth*, 100(B8), 15601–15610.

Rapp, R. P., & Watson, E. B. (1995). Dehydration melting of metabasalt at 8–32 kbar: Implications for continental growth and crust-mantle recycling. *Journal of Petrology*, 36(4), 891–931.

Rino, S., Kon, Y., Sato, W., Maruyama, S., Santosh, M., & Zhao, D. (2008). The Grenvillian and Pan-African orogens: World's largest orogenies through geologic time, and their implications on the origin of superplume. *Gondwana Research*, 14(1–2), 51–72.

Rojas-Agramonte, Y., Kröner, A., Demoux, A., Xia, X., Wang, W., Donskaya, T., Liu, D., & Sun, M. (2011). Detrital and xenocrystic zircon ages from neoproterozoic to palaeozoic arc terranes of Mongolia: Significance for the origin of crustal fragments in the Central Asian Orogenic Belt. *Gondwana Research*, 19(3), 751–763.

Rosenbaum, G. (2018). The Tasmanides: Phanerozoic tectonic evolution of eastern Australia. *Annual Review of Earth and Planetary Sciences*, 46, 291–325.

Rudnick, R. L., & Gao, S. (2003). The Composition of the Continental Crust. In H. D. Holland & K. K. Turekian (Eds.), *Treatise on Geochemistry The Crust* (Vol. 3, pp. 1–64). Elsevier-Pergamon.

Rudnick, R. L., Gao, S., Holland, H. D., & Turekian, K. K. (2003). Composition of the continental crust. *The crust*, 3, 1–64.

Ruppen, D., Knaf, A., Bussien, D., Winkler, W., Chimedtseren, A., & von Quadt, A. (2014). Restoring the Silurian to Carboniferous northern active continental margin of the Mongol–Okhotsk Ocean in Mongolia: Hangay–Hentey accretionary wedge and seamount collision. *Gondwana Research*, 25(4), 1517–1534.

Safonova, I. (2017). Juvenile versus recycled crust in the Central Asian Orogenic Belt: Implications from ocean plate stratigraphy, blueschist belts and intra-oceanic arcs. *Gondwana Research*, 47, 6–27.

Safonova, I., Perfilova, A., Obut, O., Kotler, P., Aoki, S., Komiya, T., Wang, B., & Sun, M. (2021). Traces of intra-oceanic arcs recorded in sandstones of eastern Kazakhstan: Implications from U–Pb detrital zircon ages, geochemistry, and Nd–Hf isotopes. *International Journal of Earth Sciences*, 1, 1–20.

Safonova, I., Seltmann, R., Kroner, A., Gladkochub, D., Schulmann, K., Xiao, W., Kim, J., Komiya, T., & Sun, M. (2011). A new concept of continental construction in the Central Asian Orogenic Belt. *Episodes*, 34(3), 186–196.

Safonova, I. Y., Utsunomiya, A., Kojima, S., Nakae, S., Tomurtogoo, O., Filippov, A. N., & Koizumi, K. (2009). Pacific superplume-related oceanic basalts hosted by accretionary complexes of Central Asia, Russian Far East and Japan. *Gondwana Research*, 16(3–4), 587–608.

Schandl, E. S., & Gorton, M. P. (2002). Application of high field strength elements to discriminate tectonic settings in VMS environments. *Economic geology*, 97(3), 629–642.

Şengör, A. M. C. (1990). A new model for the late Palaeozoic—Mesozoic tectonic evolution of Iran and implications for Oman. *Geological Society, London, Special Publications*, 49(1), 797–831.

Shervais, J. W. (1982). Ti-V plots and the petrogenesis of modern and ophiolitic lavas. *Earth and Planetary Science Letters*, 59(1), 101–118.

Sisson, T. W., Grove, T. L., & Coleman, D. S. (1996). Hornblende gabbro sill complex at Onion Valley, California, and a mixing origin for the Sierra Nevada batholith. *Contributions to Mineralogy and Petrology*, 126(1), 81–108.

Sisson, T. W., Ratajeski, K., Hankins, W. B., & Glazner, A. F. (2005). Voluminous granitic magmas from common basaltic sources. *Contributions to Mineralogy and Petrology*, 148(6), 635–661.

Sláma, J., Košler, J., Condon, D. J., Crowley, J. L., Gerdes, A., Hanchar, J. M., & Whitehouse, M. J. (2008). Plešovice zircon—A new natural reference material for U–Pb and Hf isotopic microanalysis. *Chemical Geology*, 249(1–2), 1–35.

Smith, E. I., Sanchez, A., Walker, J. D., & Wang, K. (1999). Geochemistry of mafic magmas in the Hurricane Volcanic field, Utah: Implications for small-and large-scale chemical variability of the lithospheric mantle. *The Journal of Geology*, 107(4), 433–448.

Söderlund, U., Patchett, P. J., Vervoort, J. D., & Isachsen, C. E. (2004). The 176Lu decay constant determined by Lu–Hf and U–Pb isotope systematics of Precambrian mafic intrusions. *Earth and Planetary Science Letters*, 219(3–4), 311–324.

Sorokin, A. A., Zaika, V. A., Kovach, V. P., Kotov, A. B., Xu, W., & Yang, H. (2020). Timing of closure of the eastern Mongol–Okhotsk Ocean: Constraints from U–Pb and Hf isotopic data of detrital zircons from metasediments along the Dzhagdy Transect. *Gondwana Research*, 81, 58–78.

Stern, R. J. (2002). Subduction zones. *Reviews of geophysics*, 40(4), 3–1.

Sun, S. S., & McDonough, W. F. (1989). Chemical and isotopic systematics of oceanic basalts: Implications for mantle composition and processes. *Geological Society, London, Special Publications*, 42(1), 313–345.

Tang, G. J., Wang, Q., Wyman, D. A., Li, Z. X., Zhao, Z. H., & Yang, Y. H. (2012). Late Carboniferous high εNd (t)–εHf (t) granitoids, enclaves and dikes in western Junggar, NW China: Ridge-subduction-related magmatism and crustal growth. *Lithos*, 140, 86–102.

Tang, J., Xu, W. L., Wang, F., Zhao, S., & Wang, W. (2016). Early Mesozoic southward subduction history of the Mongol–Okhotsk oceanic plate: Evidence from geochronology and geochemistry of Early Mesozoic intrusive rocks in the Erguna Massif, NE China. *Gondwana Research*, 31, 218–240.

Taylor, S. R., & McLennan, S. M. (1985). *The continental crust: Its composition and evolution: An Examination of the Geochemical Record Preserved in Sedimentary Rocks*. Oxford: Blackwell Science.

Tomurtogoo, O., Windley, B. F., Kröner, A., Badarch, G., & Liu, D. Y. (2005). Zircon age and occurrence of the Adaatsag ophiolite and Muron shear zone, central Mongolia: Constraints on the evolution of the Mongol–Okhotsk ocean, suture and orogen. *Journal of the Geological Society*, 162(1), 125–134.

Vermeesch, P. (2018). IsoplotR: A free and open toolbox for geochronology. *Geoscience Frontiers*, 9(5), 1479–1493.

Wiedenbeck, M., Hanchar, J. M., Peck, W. H., Sylvester, P., Valley, J., Whitehouse, M., Kronz, A., Morishita, Y., Nasdala, L., Fiebig, J., & Franchi, I. (2004). Further characterisation of the 91500 zircon crystal. *Geostandards and Geoanalytical Research*, 28(1), 9–39.

Wilhem, C., Windley, B. F., & Stampfli, G. M. (2012). The Altaids of Central Asia: A tectonic and evolutionary innovative review. *Earth-Science Reviews*, 113(3–4), 303–341.

Windley, B. F., Alexeiev, D., Xiao, W., Kröner, A., & Badarch, G. (2007). Tectonic models for accretion of the Central Asian Orogenic Belt. *Journal of the Geological Society*, 164(1), 31–47.

Windley, B. F., & Xiao, W. (2018). Ridge subduction and slab windows in the Central Asian Orogenic Belt: Tectonic implications for the evolution of an accretionary orogen. *Gondwana Research*, 61, 73–87.

Winkler, W., Bussien, D., Baatar, M., Anaad, C., & von Quadt, A. (2020). Detrital zircon provenance analysis in the central Asian orogenic belt of central and southeastern Mongolia—A Palaeotectonic model for the Mongolian Collage. *Minerals*, 10(10), 880.

Wu, F. Y., Sun, D. Y., Ge, W. C., Zhang, Y. B., Grant, M. L., Wilde, S. A., & Jahn, B. M. (2011). Geochronology of the Phanerozoic granitoids in northeastern China. *Journal of Asian Earth Sciences*, 41(1), 1–30.

Xiao, W., Windley, B. F., Hao, J., & Zhai, M. (2003). Accretion leading to collision and the Permian Solonker suture, Inner Mongolia, China: Termination of the central Asian orogenic belt. *Tectonics*, 22(6), 1–19.

Xiao, W., Windley, B. F., Sun, S., Li, J., Huang, B., Han, C., Yuan, C., Sun, M., & Chen, H. (2015). A tale of amalgamation of three Permo-Triassic collage systems in Central Asia: Oroclines, sutures, and terminal accretion. *Annual review of earth and planetary sciences*, 43, 477–507.

Yakubchuk, A. (2017). Evolution of the Central Asian orogenic supercollage since late neoproterozoic revised again. *Gondwana Research*, 47, 372–398.

Zaytsev, N. S., & Luchitsky, I. V. (1979). *Geology and magmatism of Mongolia, the joint Soviet-Mongolian scientific-research geological expedition, transactions* (Vol. 30). Nauka.

Zhao, J. H., & Zhou, M. F. (2009). Secular evolution of the neoproterozoic lithospheric mantle underneath the northern margin of the Yangtze Block, South China. *Lithos*, 107(3–4), 152–168.

Zhao, P., Appel, E., Xu, B., & Sukhbaatar, T. (2020). First paleomagnetic result from the Early Permian volcanic rocks in northeastern Mongolia: Evolutional implication for the Paleo-Asian Ocean and the Mongol-Okhotsk Ocean. *Journal of Geophysical Research: Solid Earth*, 125(2), e2019JB017338.

Zhao, P., Xu, B., & Jahn, B. M. (2017). The Mongol-Okhotsk Ocean subduction-related Permian peraluminous granites in northeastern Mongolia: Constraints from zircon U-Pb ages, whole-rock elemental and Sr-Nd-Hf isotopic compositions. *Journal of Asian Earth Sciences*, 144, 225–242.

Zhu, M., Miao, L., Zhang, F., Ganbat, A., Baatar, M., Anaad, C., Yang, S., & Wang, Z. (2022). Carboniferous magmatic records of central Mongolia and its implications for the southward subduction of the Mongol–Okhotsk Ocean. *International Geology Review*, 65, 1–20.

Zhu, M., Zhang, F., Miao, L., Baatar, M., Anaad, C., Yang, S., & Li, X. (2016). Geochronology and geochemistry of the Triassic bimodal volcanic rocks and coeval A-type granites of the Olzit area, Middle Mongolia: Implications for the tectonic evolution of Mongol–Okhotsk Ocean. *Journal of Asian Earth Sciences*, 122, 41–57.

Zhu, M. S., Zhang, F., Miao, L. C., Baatar, M., Anaad, C., Yang, S. H., & Li, X. B. (2018). The late carboniferous Khuhu Davaa ophiolite in northeastern Mongolia: Implications for the tectonic evolution of the Mongol–Okhotsk ocean. *Geological Journal*, 53(4), 1263–1278.

Zorin, Y. A. (1999). Geodynamics of the western part of the Mongolia–Okhotsk collisional belt, Trans-Baikal region (Russia) and Mongolia. *Tectonophysics*, 306(1), 33–56.

SUPPORTING INFORMATION

Additional supporting information can be found online in the Supporting Information section at the end of this article.

How to cite this article: Ganbat, A., Tsujimori, T., Miao, L., Safonova, I., Pastor-Galán, D., Anaad, C., Aoki, S., Aoki, K., & Chimedsuren, M. (2022). Age, petrogenesis, and tectonic implications of the late Permian magmatic rocks in the Middle Gobi volcanoplutonic Belt, Mongolia. *Island Arc*, 31(1), e12457. https://doi.org/10.1111/iar.12457